NASA-CR-195126

IN 72
205108
67P

RADIATIVE PROPERTIES OF MOLECULAR NITROGEN IONS PRODUCED BY HELIUM PENNING IONIZATION AND ARGON EFFECTS

By

George Miller, III, Principle Investigator
Kyo-Dong Song, Co-PI

Materials Research Laboratory
Norfolk State University
2401 Corprew Avenue
Norfolk, Virgina 23504

Interim Report
for the period September 1, '93 to February 4, '94

Prepared for the
National Aeronautics and Space Administration
Langley Research Center
Hampton, Virginia 23681-0001

Under
Research Grant NAG1-1513
Dr. Ja H. Lee, Technical Monitor
SSD-High Energy Science Branch

February 4, 1994

SUMMARY

The development of hypersonic aerospace vehicles requires a better understanding on the thermal and chemical nonequilibrium kinetics of participating species in shock layers. The computational fluid dynamic (CFD) codes developed for such flowfields overestimates the radiation in the spectral region of 300 - 600 nm. A speculation for this overestimation is that inclusion of Ar, CO_2, and H_2O at the upper atmosphere flight region makes a significant impact on radiative kinetics of molecular nitrogen ions.

To define the effects of minority species on the radiative kinetics of N_2^+, an experimental setup was made by using the helium Penning ionization. The vibrational and rotational temperature were measured by mapping the vibrational and rotational distributions of N_2^+ emission with high spectroscopic resolution and absolute intensity measurements. Measured vibrational temperatures were in the range from 18,000 to 36,000 K, and rotational temperatures were in the range from 300 to 370 K. The irradiance of 391.44 nm line and rotational and vibrational temperatures were analyzed to define argon and CO_2 effects on the N_2^+ emission. When Ar or CO_2 is injected with N_2, the rotational temperature did not change. The irradiance were reduced by 34% and 78% for the 50% of mixture of Ar and CO_2, respectively. The vibrational temperature were increased by 24.1% and 82.9% for the 50% of mixture of Ar and CO_2, respectively. It appears that there are no significant effects from small concentrations of Ar and CO_2 at the upper atmosphere flight region.

CONTENTS

1. INTRODUCTION

2. THEORETICAL BACKGROUND

3. EXPERIMENT

4. RESULTS AND DISCUSSION

LIST OF FIGURES

LIST OF TABLES

1. INTRODUCTION

1-1. Background

Recent interest in the development of hypersonic flight vehicles such as the National Aerospace Plane (NASP) and Aero-assisted Orbital Transport Vehicle (AOTV) have required accurate data bases to simulate thermally and chemically nonequilibrium hypersonic flows with computational fluid dynamic (CFD) codes. The CFD code is able to predict the heating load needed for designing the thermal protection system of aerospace vehicles encountering hypersonic flows. The radiative heat load on a vehicle moving through the upper atmosphere increases as the velocity and size increase and accurate prediction of radiative as well as convective heating becomes important to mission planners and vehicle designers.

The flow field around such a hypersonic vehicle is difficult to simulate[1] in a ground-based facility because of the low density and high enthalpy nature of the flow involved. Therefore, radiative heating predictions depend upon flowfields obtained from nonequlibrium CFD codes, such as LAURA (the Langley Aerothermodynamic Upwind Relaxation Algorithm)[2] and LORAN (the Langley Optimized Radiative Nonequilibrium)[3] codes. These flowfield solvers contain energy exchange models that have yet to be validated. Although perturbations in these models may have little effect on convective heating, their effect on the radiative heating level can be large. The recent evaluation of the FIRE II flight data for radiation[4] shows that the prediction made by these codes overestimate the radiation in the spectral region of 300 - 600 nm where N_2^+ first negative-band emission is dominant as shown in figure 1. In this figure, the N_2^+ first negative band head (391.44 nm) can be identified in the radiation spectrum predicted by the LAURA-LORAN codes but not in that measured by the FIRE II flight. This is an important point to note because the CFD codes must predict the dominant radiation load to hypersonic or hypervelocity aerospace vehicles coming from molecular ions such as N_2^+, O_2^+, NO^+, etc. produced within nonequilibrium shock layers. Especially, the excited molecular nitrogen ion, N_2^{+*}, appears to be a major contributing species for radiation flux according to the solution of the CFD code developed for a simulation of FIRE II flight experiment.

To resolve the over-estimation of LAURA and LORAN codes for the FIRE II flight in a high altitude range (> 60 Km), a possibility could be pointed out for that inclusion of argon (0.9 %), CO_2 (0.03%), H_2O ($\approx$1%) existing in the

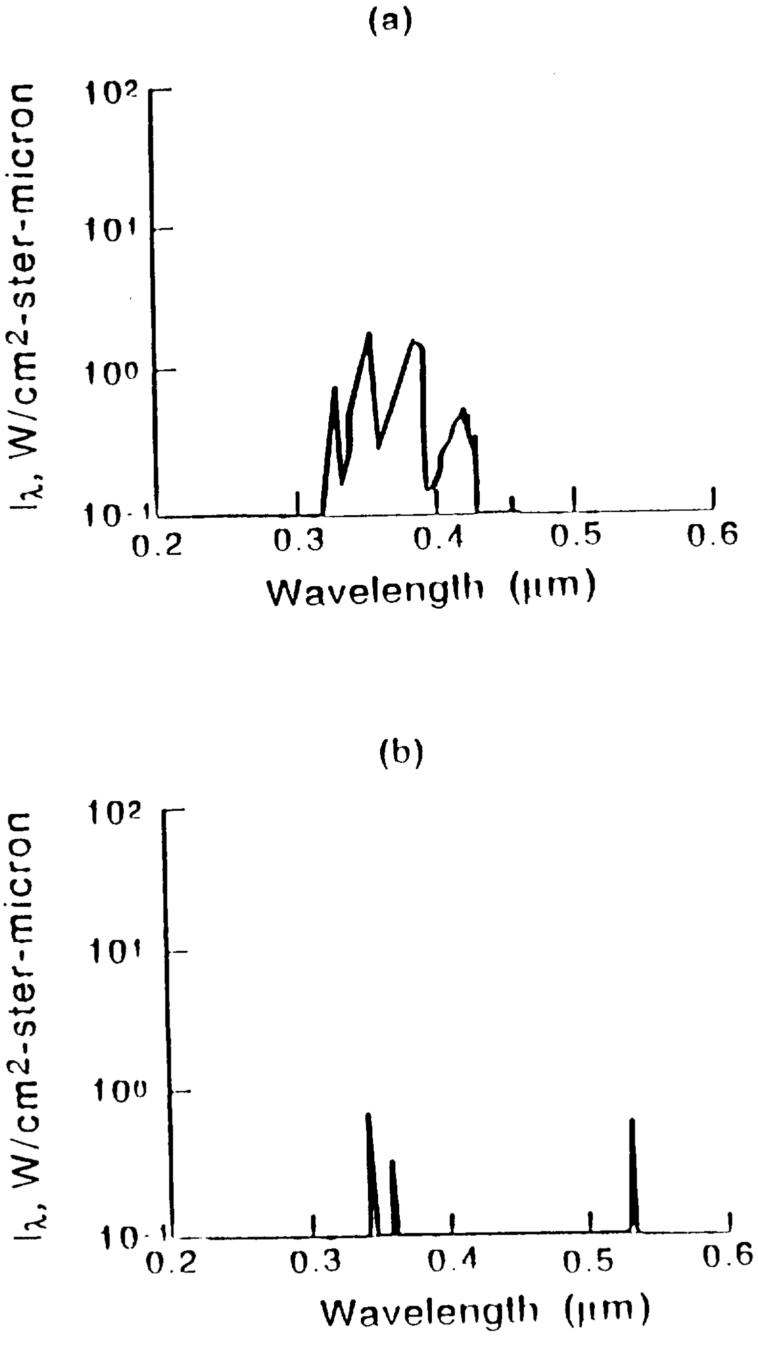

Figure 1. The predicted (a) and measured (b) radiation spectra of the FIRE-II flight taken from reference 2, 3, and 4.

upper atmosphere might make a difference in radiative properties of molecular nitrogen ions. However, the possibility of argon and other species effects on radiative properties of molecular ions has never been considered in the CFD code or in any ground windtunnel experiments. Recently, the emission intensity reduction by about 10% for the first negative system of N_2^+ with real atmospheric pressure air was reported by Laux etc.[5], but the contribution of each minority species was not examined. For example, molecular nitrogen and argon have very similar ionization potential as shown in figure 2, so that the nitrogen and argon ions, N_2^+ and Ar^+, may be competitively produced by electron impact or quenched by very fast charge exchange reactions.

In this research, N_2^+ was produced by using the helium Penning ionization (PI). The process of Penning ionization was first postulated in 1927 by F. M. Penning [6] to explain the lowering of the breakdown voltage in rare-gas discharges when a small amount of impurities was added. The common theme in the various classical, semiclassical, and quantum mechanical approaches to PI is the two-state potential-curve model proposed by Herman and Cermak [7] in 1966. The reaction processes of triplet metastable helium atoms (19.72 eV) with N_2 have been exploited by Hotop and Niehaus. [8] The generation of $He(2^3S)$ by a hollow cathode discharge coupled to a flow apparatus was described, and with this apparatus the PI reaction of $He(2^3S)$ with molecular nitrogen was investigated at pressure of 1 - 5 torr of helium and less than 1 mtorr of N_2 at 300, 225, and 77 K by Richardson and Setser [9] in 1973.

The rate coefficient for chemiluminescent reactions of exited helium with N_2 was determined in 1968 by Cher et al. [10], and they reported that the rate coefficient was approximately proportional to the temperature over the range 305 - 527 K, and was $(1.0 \pm 0.3) \times 10^{-10}$ cm^3 $molecule^{-1}$ sec^{-1} at 300 K and 1 - 2 torr of He pressure. The rate coefficients for the reaction $N_2^+ + Ar \rightarrow Ar^+ + N_2$ were obtained by many researchers.[11 - 14] Their experimental methods and results are shown in table 1. The Penning ionization cross section for collisions of $He(2^3S)$ metastable atoms with N_2 was measured as 5 Å in 1969 by Bolden et al.[15] Also they reported that the ionization probability of N_2 per collision was 0.07, and their results for cross section and ionization probability agreed with the previous experimental results of Bell et al.[16]

In most CFD codes for shock layer simulations great emphasis is placed on the two-temperature model, in which it is assumed that the translational and rotational energy modes are in equilibrium at the translational temperature, and vibrational, electronic, and electron translational energy modes are in equilibrium at the vibrational temperature . Consequently, the

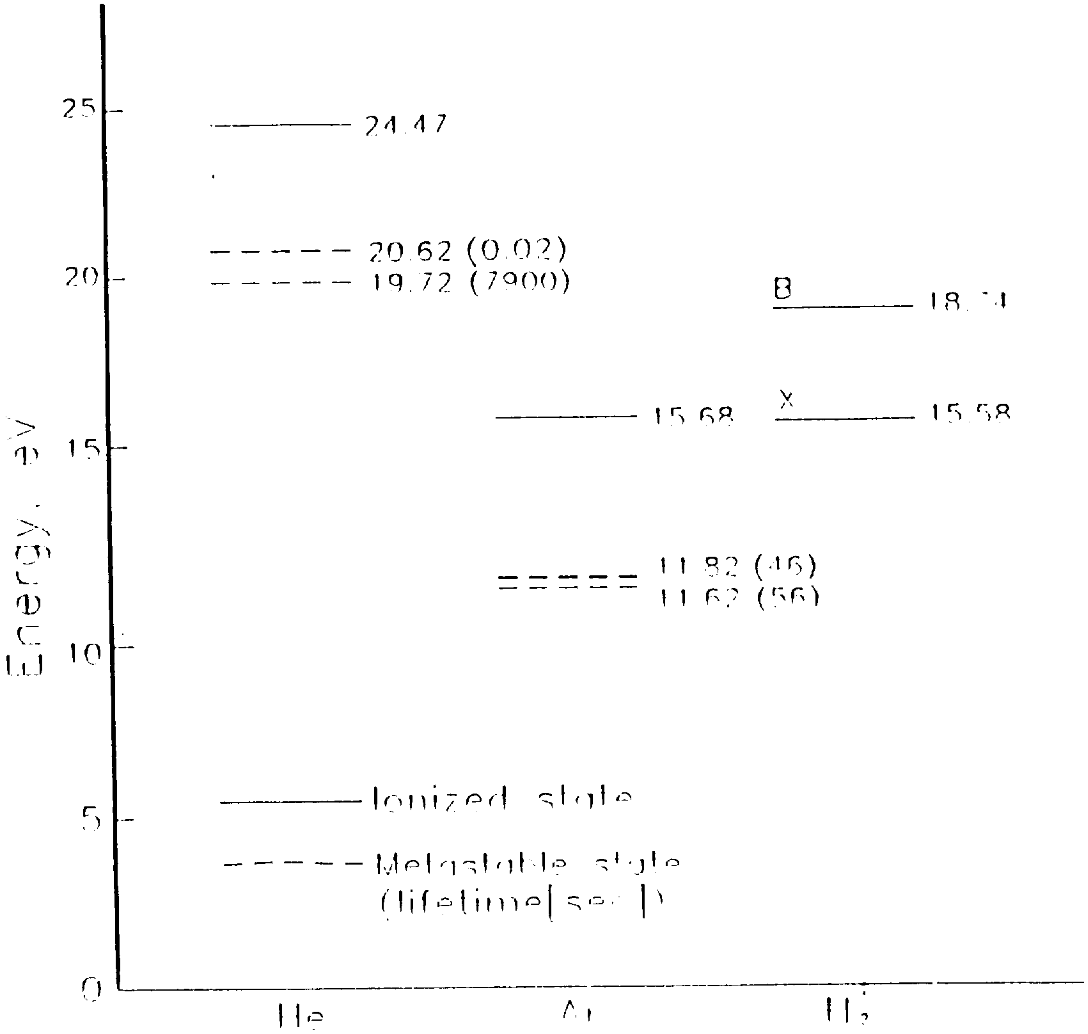

Figure 2. Energy levels for ionization and metastable state of He, Ar, and N_2^+

ORIGINAL PAGE IS
OF POOR QUALITY

Rate Coefficient (10^{-11} cm^{3}sec^{-1})	Method	Authors
0.2 - 1.5	Drift tube	Howorka[11]
0.1 - 0.4	Stationary afterglow	Adams[12]
0.25	Flowing afterglow	Hyatt[13]
1 - 70	Drift tube	Lindinger[14]

Table 1. Rate coefficients for reaction of molecular nitrogen ions with Ar obtained at about 300 K.

rotational temperature is higher than the vibrational temperature in the CFD codes. However a disagreement of the vibrational and rotational temperatures in the atmospheric layers with a higher vibrational temperature was cited by Herzberg[17] in 1950 without providing a clear reason for the discrepancy. Similar disagreement near a shock layer was also reported recently by Blackwell.[18] It was thought to result from conditions ahead of the shock caused perhaps by differences in rotational relaxation in the heated and expanded arc jet flow. Recently, he reported [19] the rotational and vibrational temperature differences in arc jet shock layers as 12,000 K and 5,500 K for vibrational and rotational temperatures respectively. Also, recently reported [20] shock tube measurements have shown that the rotational temperature was lower than the vibrational temperature at the shock front.

To execute Penning ionization, it is necessary to produce metastable atoms. Because of its long life time (7900 sec) [21] and having a similar potential energy as molecular nitrogen ions, helium metastable atoms were selected in this research. The helium matastable atoms were made by Hollow-cathode glow discharges, a most common technology.

1-2. Purpose of Research

To re-examine the radiative properties of nitrogen molecular ions, the excited N_2^+ will be generated by using the helium Penning ionization method with hollow-cathode discharge. To reveal the variations of the vibrational and rotational temperatures for different operation conditions, the vibrational and rotational spectral distributions with high spectral resolution and absolute intensity measurements will be made. The rate coefficients and collisional cross-sections of the attendant reactions will be evaluated with the measured data. Also, the argon and CO_2 effects on radiative properties of N_2^+ will be determined.

2. THEORETICAL ANALYSIS

2-1. The Hollow-Cathode Discharge

For a long time the hollow-cathode discharge has been utilized as a source of line radiation from light and heavy elements with a relatively high intensity and sharp spectral lines. The hollow- cathode discharge is basically a gas glow discharge, and the observation is usually made at the positive column. In figure 3(a) [22] glow discharge is sketched. There are four dark regions, Aston, Cathode, Faraday, and Anode dark space, and four light emitting regions, Cathode glow, Negative glow, Positive colimn, and Anode glow. Most parts are occupied by the negative glow and the positive column. The intensity of the spontaneous emission is not very high because the current must be limited to keep the discharge stable in the glow discharge range. The current density at the cathode surface increases two or three orders of magnitude when the negative glows develop in a hollow cathode at a constant cathode-anode voltage. The intensity of the emission from this glow also increases strongly. This type of discharge is called a hollow cathode discharge as shown in figure 3(b). Its main feature is that the negative glow is captured inside the cathode.

When the current i in a discharge of moderate length is raised further, the discharge voltage first decreases rapidly and then at a slower rate until it reaches a constant voltage, the normal cathode fall V_n. In table 2 values [22] are given for various combination of the gases and cathodes. The thickness of the cathode dark space which varies inversely with pressure for a constant gas temperature is another important parameter. In helium glow discharge, Pd_n is 1.32, 1.30, and 1.45 for Al, Fe, and Mg respectively [22], where P is pressure and d_n is electrode spacing.

The energy level diagram for helium is shown in figure 4.[23] The term system of He splits essentially into two partial systems, which do not combine radiatively with each other. In particular, the lowest state of triplet, 2^3S, which lies 19.72 eV above the ground state, and 1^1S, are forbiden to transfer to the ground state. Those terms which can not go to a lower state with emission of radiation, and can not be reached from a lower state by absorption are called metastable states. However the helium in low-voltage glow discharge can be excited to any level which undergoes transition to a 16metastable state by radiative recombination

$$He + e \rightarrow He^{**} + e. \qquad (1\text{-a})$$
$$He^{**} \rightarrow He^{*} + h\nu \ (388.9 \text{ nm}) \qquad (1\text{-b})$$

In the radiative transitions, 318.8 nm($4^3P \rightarrow 2^3S$), 388.9 nm ($3^3P \rightarrow 2^3S$), and 1082.9 nm($2^3P \rightarrow 2^3S$) emissions can be seen, and the line of 388.9 nm is the strongest emission.

2-2. Penning Ionization

When a metastable rare-gas atom X^* collides with another atom Y or a

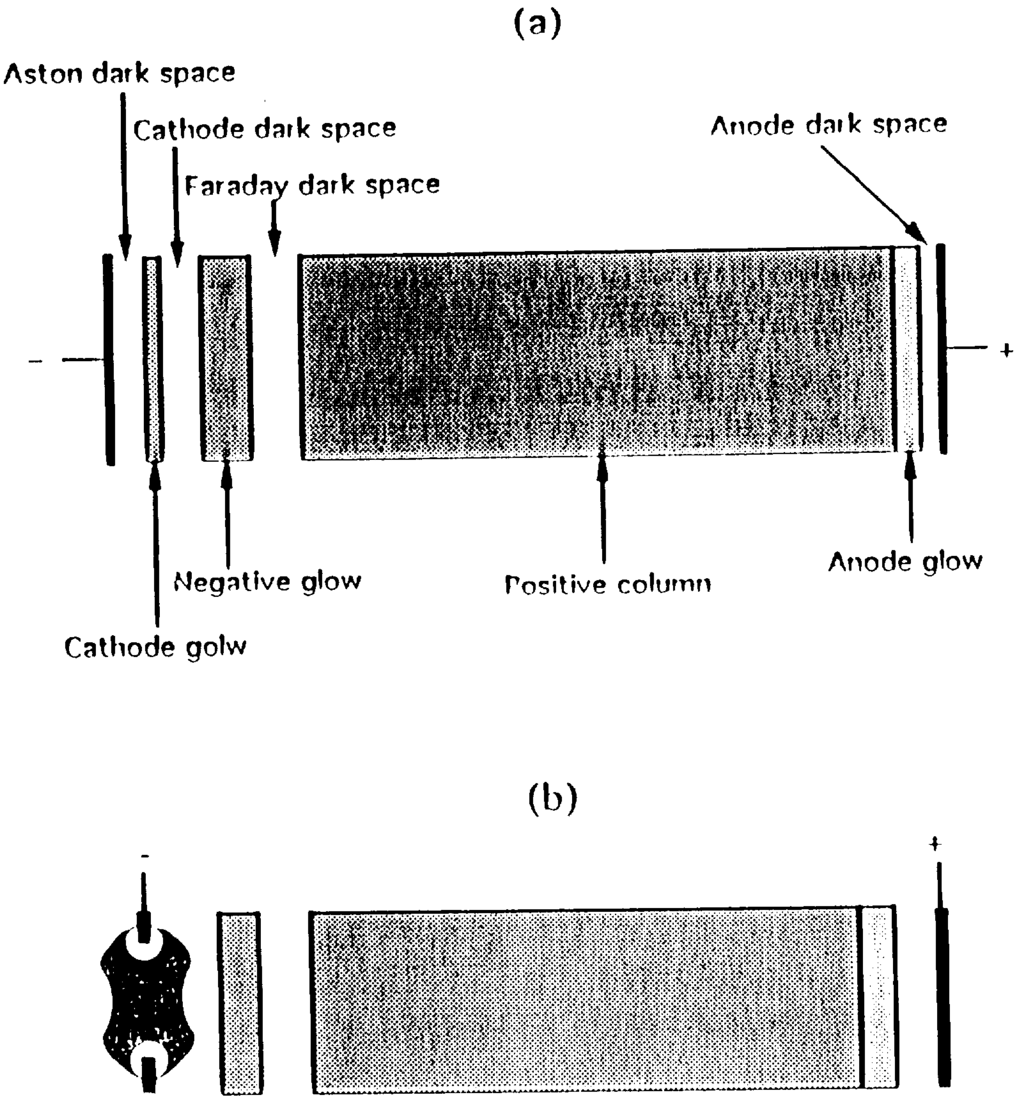

Figure 3. The glow discharge (a) with a planer cathode, and (b) with a hollow-cathode. 22

Gas / Cathode	A	N_2	H_2	He	Hg	Air
Al	100	120	170	140	245	229
Ba	93			86		
Fe	165	150	250	180	298	269
Mg	119	94	153	125		224
Ni	130	140	211	158	275	226

Table 2. The values of the normal cathode fall (V_n). [22]

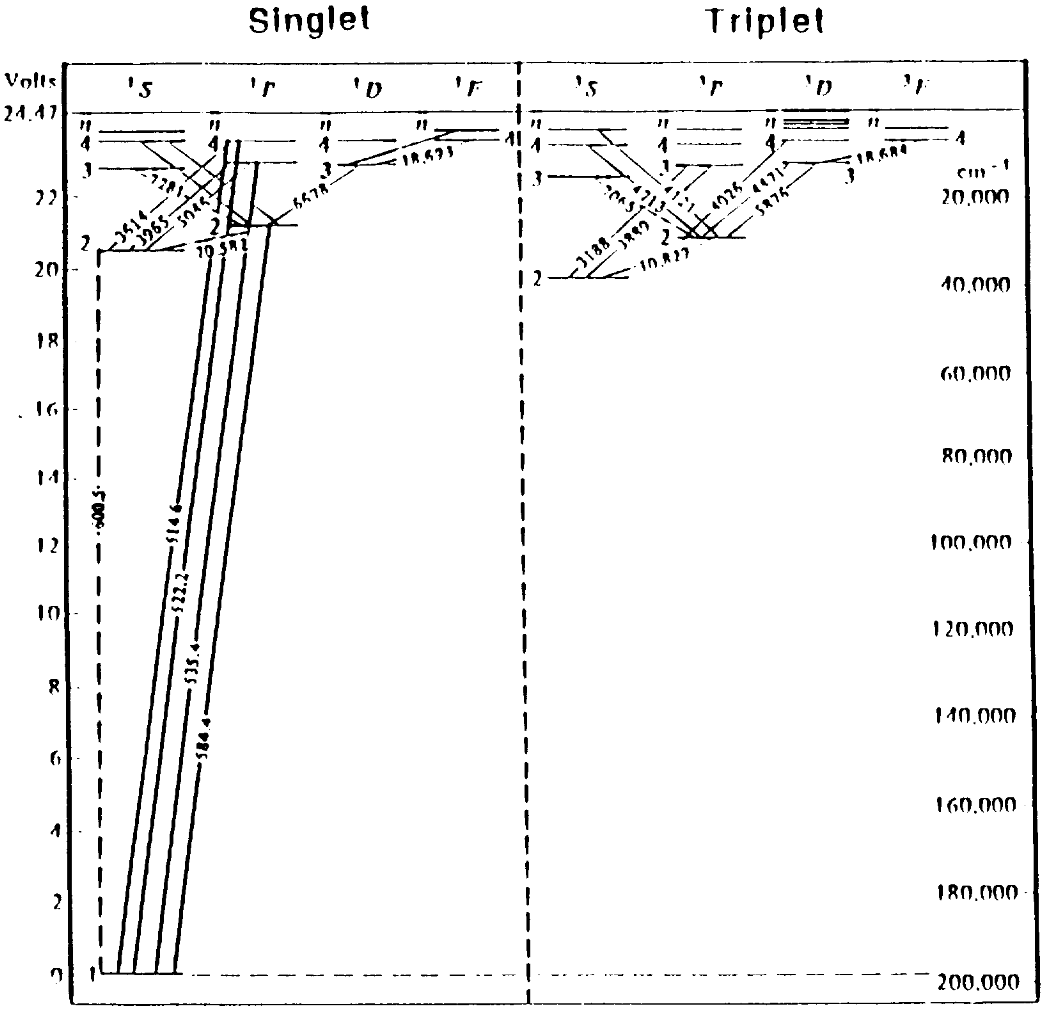

Figure 4. Energy levels diagram for helium. 23

molecule AB, several reaction channels are potentially possible. If the electronic energy available in the metastable atom exceeds the lowest ionization potential of the atom or molecule, the process known as Penning ionization can occur:

$$X^* + Y \rightarrow X + Y^+ + e^- \qquad (2\text{-a})$$
$$X^* + AB \rightarrow X + AB^+ + e^- \qquad (2\text{-b})$$

The model for Penning ionization is summarized with the aid of figure 5.[9] The upper curve represents the incoming reactant channel that lies in the ionization continuum of the outgoing product channel given by the lower three curves. Although not shown in figure 5, the ionizing transitions occur to a range of vibrational and rotational levels of the ion. The kinetic energy[10] of an electron arising from a transition at the separation R between N_2 and He is

$$E_k = [\ V(He^*,N_2) + E_J - V(He,N_2^{+*}) - E_{v'}{}^+ - E_{J'}{}^+]_R. \qquad (3)$$

The vibrational and rotational quantum numbers of N_2^+ are denoted by v' and J', and J is the rotational quantum number of N_2.

The process is illustrated by the reactions of He (2^3S,19.72 eV) with N_2:

$$\begin{aligned} He\ (2^3S) + N_2 &\rightarrow N_2^+ + He + e^-\ (40\%) \\ &\rightarrow N^+ + N + He + e^-\ (60\%), \end{aligned}$$

and the product distribution has been determined by Adams[24] at 300 K. When the excited molecular nitrogen ion , $N_2^+(B^2\Sigma_u^+)$, decays to ground state, $N_2^+(X^2\Sigma_g^+)$, the bandhead wavelength of emission is 391.44 nm. The other prominent emissions which are from different vibrational levels are in table 3.

2-3. Vibrational and Rotational Temperature

For any mode of excitation which results in a Boltzmann distribution, the intensity distribution of a molecular band system in which the population of the vibrational energy levels is given by[25]

$$I_{v'v''} = (ANS_{v'v''}/g_{v'}\lambda^4)\exp(-E_v/kT_v) \qquad (4)$$

where A is a constant determined by the experimental optical configuration,

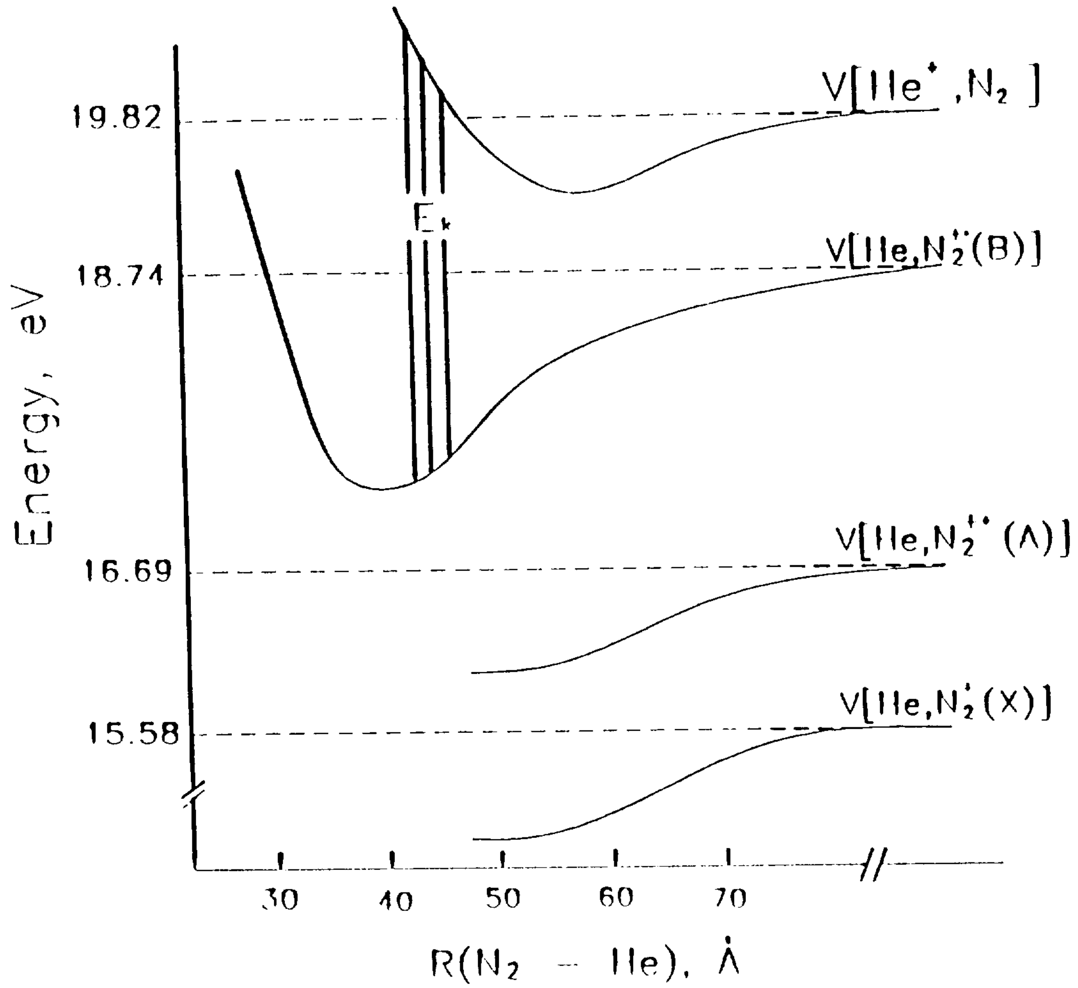

Figure 5. Schematic representation of the model for Penning Ionization. 9

Wavelength (nm)	Transition	
	Electronic	Vibrational
391.44	N_2^+, B-X	0 - 0
427.81		0 - 1
470.92		0 - 2
358.21		1 - 0
388.43		1 - 1

Table 3. The prominent emissions of N_2^+, B-X system.

N is the population of the vibrational ground state, $S_{v'v''}$ is the band strength for the transition, l is the wavelength of the emitted spectral line, E_v is the energy of the upper state, and T_v is the vibrational temperature. A plot of $\ln(I_{v'v''}/S_{v'v''})$ as a function of E_v yields a straight line with a slope equal to $-1/kT_v$.

For more practical applications, we can write as [26]

$$T_v = 1.4388\ \Delta E_i(\mathrm{cm}^{-1})/\ln(I_1/I_0) \tag{5}$$

if two absolute intensities of vibrational transitions, $I_1$of (1-0) and I_0 of (0-0) line of molecular nitrogen ions, are measured. In equation (5), $\Delta E_i(\mathrm{cm}^{-1})$ is equal to E_0-E_1.

The rotational temperature is calculated as follow. From the Bolzmann distribution law, the number of molecules $N_{J'}$ in the rotational level J' at rotational temperature T_R is [25]

$$N_J = (2J'+1) \exp[-J'(J'+1)/kT_R] \tag{6}$$

where k is the Boltzmann constant and T_R is the rotational temperature. The fluorescence intensity of the rotational transition depends on the mean value, J'+J"+1, of 2J+1 for the upper and lower states. Therefore, the line intensity distribution with a molecular band is given by

$$I_{J'J''} = A\ (J'+J''+1) \exp[-J'(J'+1)/kT_R] \tag{7}$$

where $I_{J'J''}$ is the intensity of the emitted spectral line, J' and J" refer to the upper and lower rotational quantum numbers of the transition, T_R is the rotational temperature, and A is a constant determined by the experimental optical configuration. A rotational temperature may be extracted from the relative rotational line intensities by plotting the logarithm of the quantity $I_{J',J''}/(J'+J''+1)$ versus J'(J'+1). The plot yields a straight line for a Boltzmann distribution whose slope is proportional to the reciprocal of the absolute temperature.

2-4. Collisional Cross-Section and Rate Coefficient.

The collision cross section is calculated from [27]

$$s = S/[N(N_2)N(He^*)v] \tag{8}$$

where $N(N_2)$ and $N(He^*)$ are the number density of N_2 and He^* respectively, v is the mean thermal velocity, and s is the collision cross section. Because the detected emission intensity is proportional to the rate of population of the excited state of nitrogen molecular ions, and v is constant when temperature is fixed, the collision cross section can be determined from the slope of I vs. N(N2) with same production of He*.

The calculation of the rate coefficient for the reaction populating the emitting state is based on the assumption that the emission intensity is proportional to the rate of the energy transfer reaction. For example, in the case of N_2, assuming the excited helium species is the 2^3S, the intensity from process (9) is proportional to the rate of the Penning reaction

$$He^*(2^3S) + N_2 \rightarrow N_2^+(B^2\Sigma_u^+) + e^- + He \qquad (9)$$

$$N_2^+(B^2\Sigma_u^+) \rightarrow N_2^+(B^2\Sigma_u^+) + h\nu \qquad (10)$$

Since the concentration of N_2 is in large excess, the intensity is proportional to the concentration of He^*. The two mechanisms considered for the disappearance of He^* are diffusion to the walls where the concentration is set at zero. The solution of the mass balance equation in a cylindrical reactor for laminar flow and a parabolic velocity profile has been worked out [28] and the result was

$$-d(\ln I)/dx = [(D_0p_0)\pi]/[760\Sigma F\, RT]\,(\lambda_0^2/2) + k_1\pi[(pr_0)/(\Sigma F\, RT)]^2[(1-\varepsilon)/2]F_N \qquad (11)$$

where I is the emission intensity, x is the axial distance, D_0p_0 is the diffusion coefficient of the excited helium, ΣF is the total flowrate in moles/sec, R is the gas constant, T is the temperature, p is the average pressure, r_0 is the radius of the tube, F_N is the flow rate of the reactant gas, and λ_0, ε, and π are numerical constants equal to 2.710, 0.237, and 3.14 respectively. The rate coefficient k_1 is obtained from the measurement of intensity as a function of distance by plotting d(lnI)/dx vs. F_N.The calculation of the rate coefficient for the reaction populating the emitting state is based on the assumption that the emission intensity is proportional to the rate of the energy transfer reaction.

With the argon mixture, the following reaction occurred.

$$He^* + Ar \rightarrow He + Ar^+ + e \qquad (12)$$

$$N_2^+ + Ar \rightarrow N_2 + Ar^+ \quad \text{(ground-state ion reaction)} \qquad (13)$$

$$N_2^{+*} + Ar \rightarrow N_2^+ + Ar \quad \text{(molecular ion reaction)} \qquad (14)$$

The chemical reaction (12) and (14) will reduce the number density of N_2^+, and (13) can reduce or increase that. If there is no ground-state reaction then the ion balance equation will be [29]

$$d[N_2^{+*}]/dt = -k[Ar][N_2^{+*}] \tag{15}$$

where k is the rate coefficient, [Ar] and $[N_2^{+*}]$ are the population of the argon and molecular nitrogen ion respectively. The corresponding solution is then

$$[N_2^{+*}] = [N_{2(0)}^{+*}] \exp(-k[Ar]t) \tag{16}$$

where $[N_{2(0)}^{+*}]$ is the initial molecular ion population. Because the emission (391.44 nm) intensity is proportional to the number density of N_2^{+*} equation (16) will be

$$I/I_0 = \exp(-k[Ar]t) \tag{17}$$

where I is the emission intensity of 391.44 nm line after argon gas is added, and I_0 is the initial intensity of the same line. The rate coefficient of the reaction, k, is obtained by the curve fitting of emission intensity vs. argon flowrate. In this coefficient, the rate coefficient of the reaction (9) and (12) are included.

3. EXPERIMENTAL ARRANGEMENT

The experimental arrangement for this research is shown in figure 6. The experimental system is constituted by two main parts, the reaction chamber and the detection system.

3-1. Reaction Chamber

The reaction chamber has an inlet for helium gas, a pair of hollow-cathode discharge electrodes and a neutralizer grid electrode, an inlet for nitrogen gas or a mixture of nitrogen and argon gases, and an outlet port for

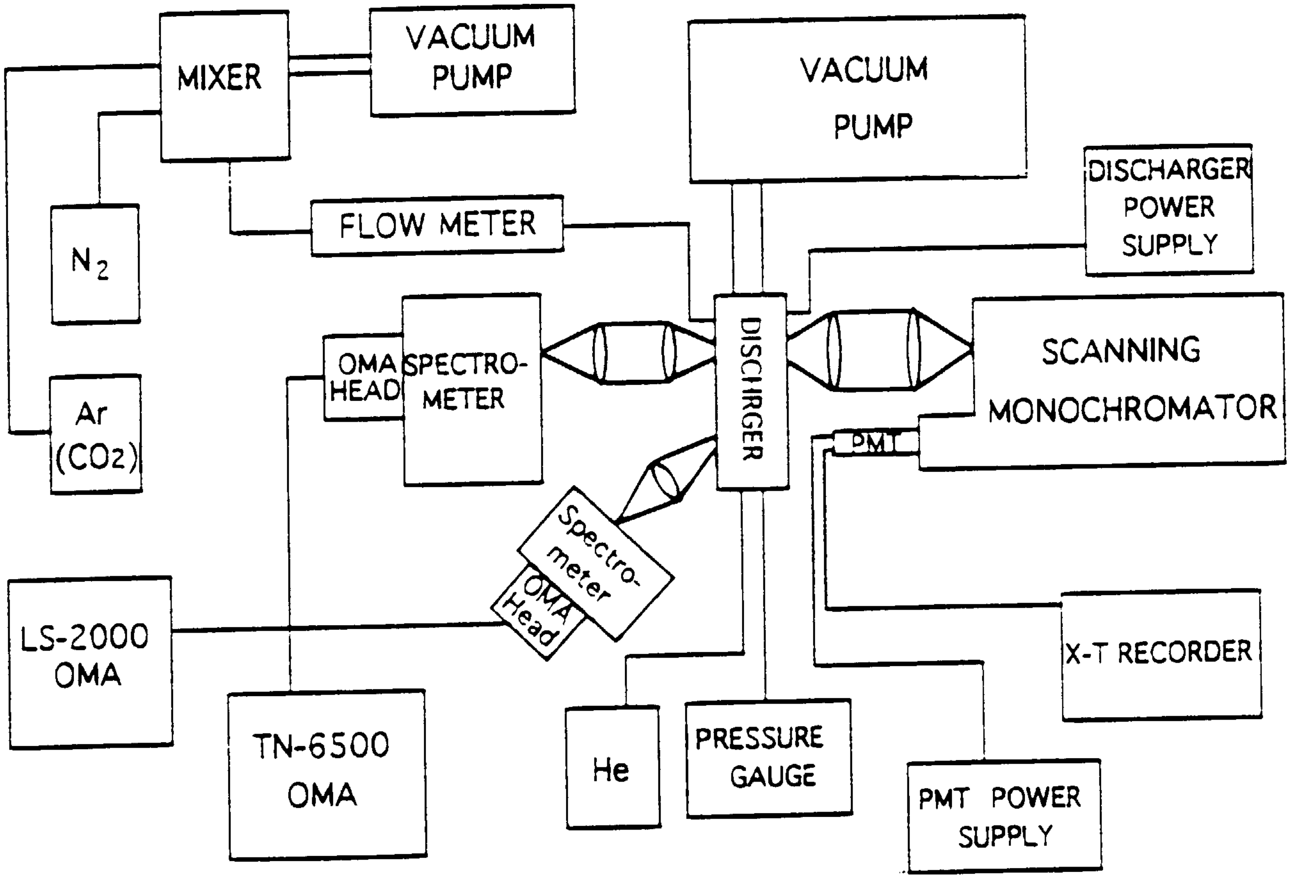

Figure 6. The schematic of the experimental arrangement.

vacuum pump. As shown in figure 7 the aluminum electrodes are placed inside the 10-cm diameter plexiglass vacuum chamber. Two discharge electrodes have a hollow tube shape and the same diameter of 13 mm. The hollow cathode which directly faces the helium inlet is 8-mm long, and a 13-mm long positive electrode is located next to the hollow- cathode with about 10-mm apart. And the diameter of neutralizer grid electrode is 50 mm. This electrode is to neutralize the discharged He bycapture the He^+ which is made at the hollow-cathode discharge region. A compartment which has a hole of 20-mm of diameter at the center is employed between the grid electrode and nitrogen inlet to increase the flow velocity of He^* and to decrease the diffusion of nitrogen gas to hollow-cathode discharge region.

Helium gas was controlled by a micro-valve to maintain a desired chamber pressure (0.7 - 2.0 torr), and the chamber pressure was measured by the Hastings Vaccum Gauge SP-1. The flow of nitrogen or mixed (nitrogen + argon or CO_2) gas was controlled by the Matheson Mass Flowmeter. The mixed gas was made in the mixing chamber which is connected with nitrogen and argon (or CO_2) containers. Each regulated gas by the Parametrics Electronic Manometer 1174 were inserted to the mixing chamber, and mixed by a fan which is controlled by Black & Decker 3/4 hp motor and Variac W5MT3 Autotransformer. The pressure of the mixing chamber was measured by the Wallace & Tiernan Absolute Pressure Gauge. A vacuum pump (General Electric, 1/3 hp) was connected to the mixing chamber to make it vacuous before the new mixed gas was made. Since helium and nitrogen gases are continuously injected, the chamber is continuously pumped out by two mechanical pump (Veeco RG-31X and General Electric Vacuum Pump) to maintain a desired chamber pressure.

The power supply, Canberra 3000 High Voltage Power Supply, provides power in the range of 250 - 600 V and 1 - 8.4 mA to sustain a helium hollow-cathode discharge between two electrodes. Five resistors (12, 12, 12, 24, and 24 kΩ) were connected at the output of power supply in the series to change the current at the same voltage.

Although the main reaction in the glow is $He + e \rightarrow He^* + e$, aportion of the electron-impacted helium will be ionized ($He + e \rightarrow He^+ + 2e$). The portion passing through the ion neutralizer electrode is neutralized. After this neutralizer electrode, nitrogen gas is injected into the ion-free stream of metastable helium atoms to achieve the Penning ionization.

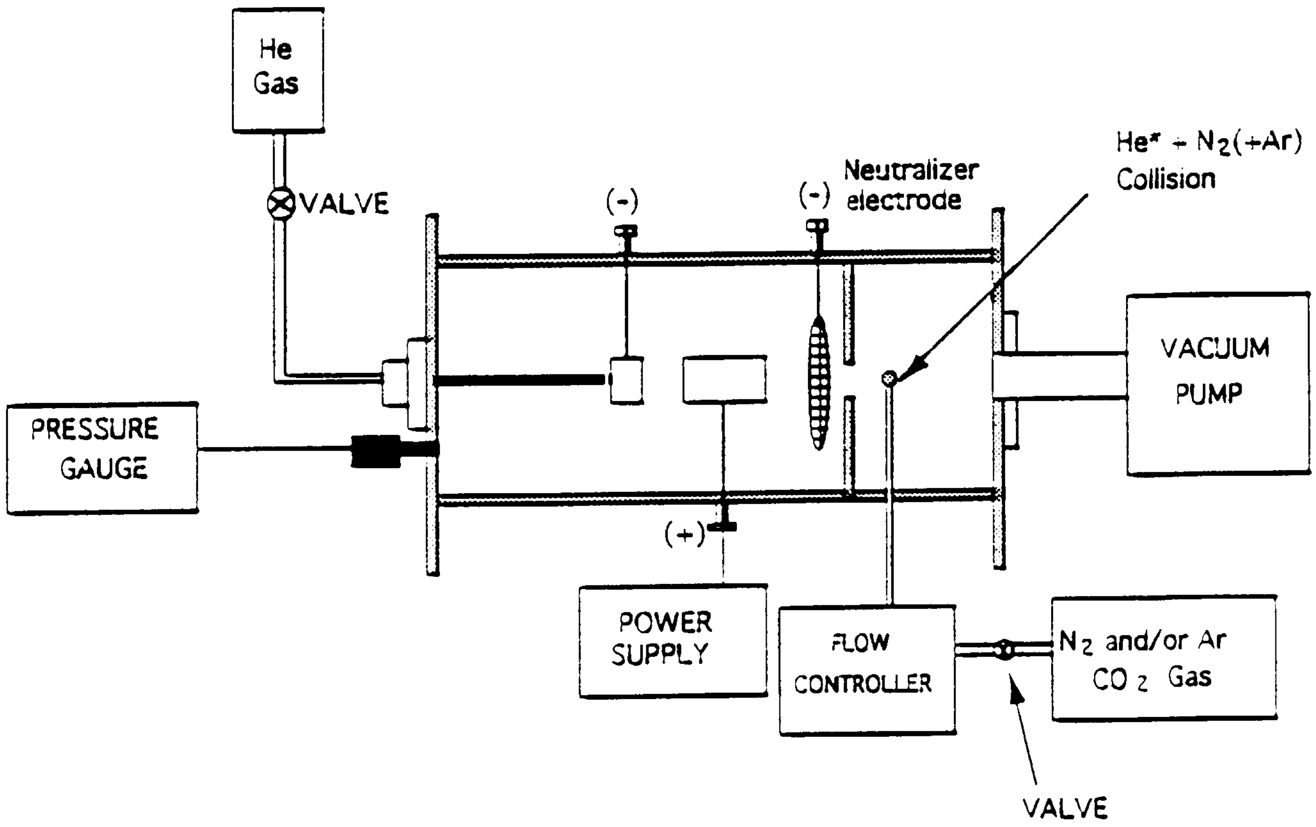

Figure 7. The reaction chamber.

3-2. Detection System

Three line emission spectra were diagnosed and the arrangement of instruments is shown in figure 8. One of the transitions with the line emission at 388.91 nm was used for monitoring He* production by the combination of the Jarrell Ash 0.25-m spectrometer and the Lamda LS-2000 optical multichannel analyzer (OMA). The grating of the spectrometer was blazed for 300 nm and had 590 groove/mm which resulted in a linear dispersion of 6 nm/mm (first order). The entrance slit was 20 mm. The emission from 363 to 468 nm was detected (Fig. 9) at the hollow-cathode discharge region (between two electrodes). The 388.91 nm ($3^3P \rightarrow 2^3S$), 396.47 nm ($3^1P \rightarrow 2^1S$), 402.62 nm ($4^3D \rightarrow 2^3P$), and 447.10 nm ($3^3D \rightarrow 2^3P$) lines were detected at the condition of 500 V of the discharge voltage, 3.75 mA of current, and 1.0 torr of He pressure. The 388.91 nm line was monitored by the temporal mode of the OMA during the data taking to monitor the stability of He* production (Fig. 10). Because one scan takes two second, the figure shows the production of He* was stable at least for 200 seconds. The variation of the line intensity was ±2 % of the average at this condition.

To determine vibrational temperatures, the first negative band of N_2^+ near 391.4 nm was resolved where by the combination of the Jarrell Ash 0.27-m spectrometer and the Tracor Northern TN-6500 OMA. The grating used was blazed for 400 nm and had 600 groove/mm which resulted in a linear dispersion of 6 nm/mm. The distance between the detection point and the entrance slit of the spectrometer was 48 cm, and the slit width was 25 mm. The emitted light was collected by two quartz lenses and focused onto the entrance of the spectrometer. The detection range of the system was from 328.35 nm to 480.18 nm. For the vibrational temperature measurement, $N_2^+(0\text{-}0)$ and $N_2^+(1\text{-}0)$ lines weredetected with absolute intensity calibration by the EG & G GS-900 standard source. The calibration factors will be discussed in the next chapter. The lineality of the OMA head was tested, and the result is shown in figure 11. The result shows that the intensity is linear from 388 to 13 counts. Therefore the calibration factor for the lineality of photodiodes in the OMA head is the unity in this count range.

To measure the rotational temperature, the combination of the McPherson 0.5-m scanning monochromator and the Pacific Photometric RCA

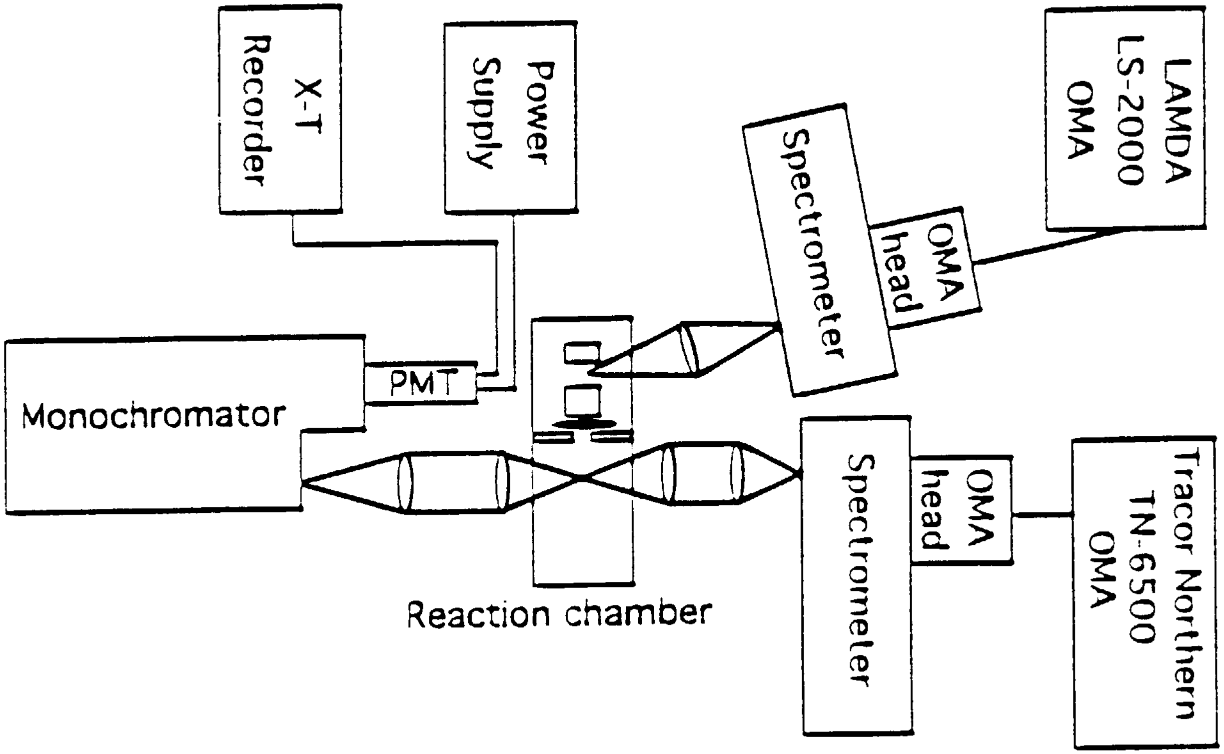

Figure 8. The arrangement of the detection system.

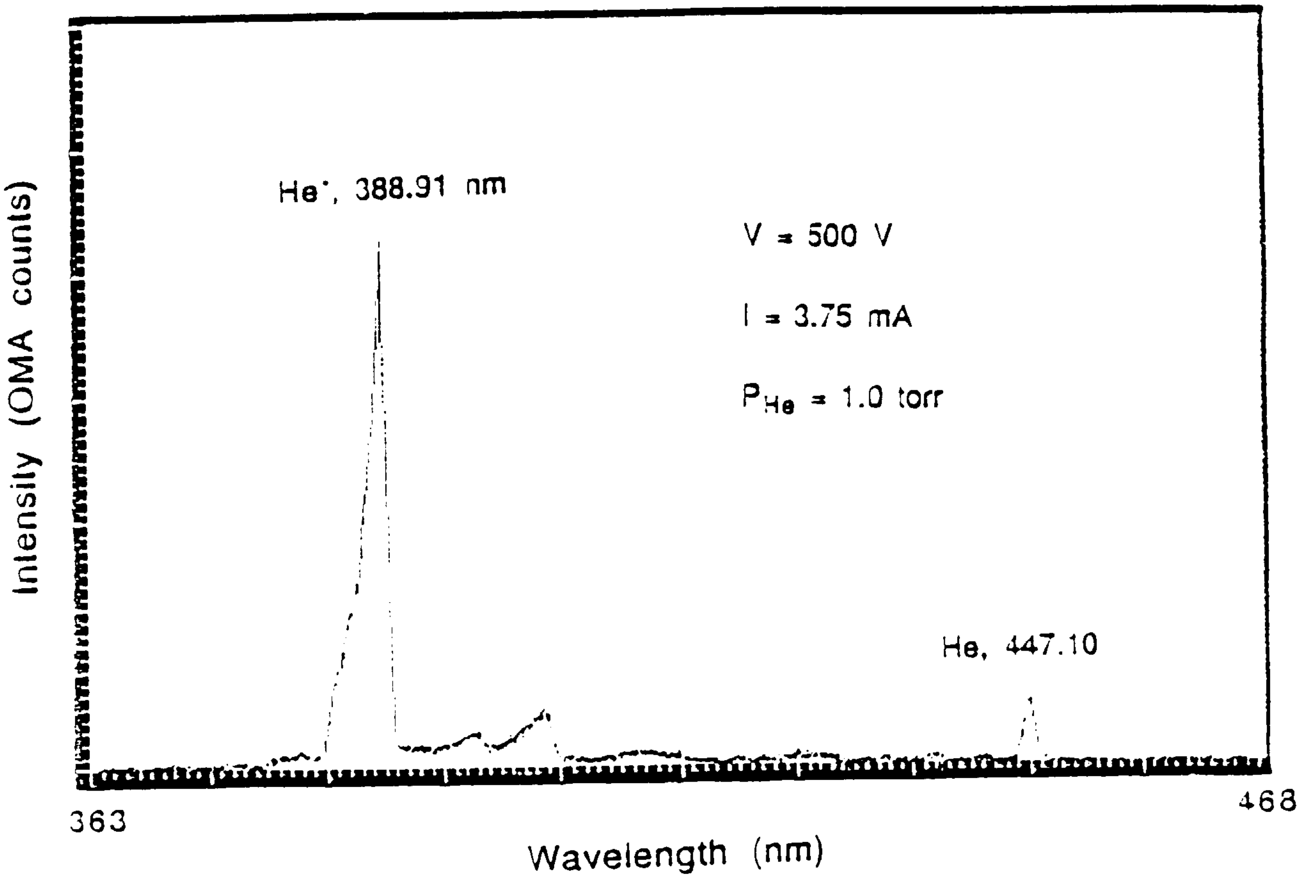

Figure 9. The spectrum acquired with Lamda LS-2000 at the conditions of 1-torr He, 500-V of discharge voltage and 3.75 mA of current.

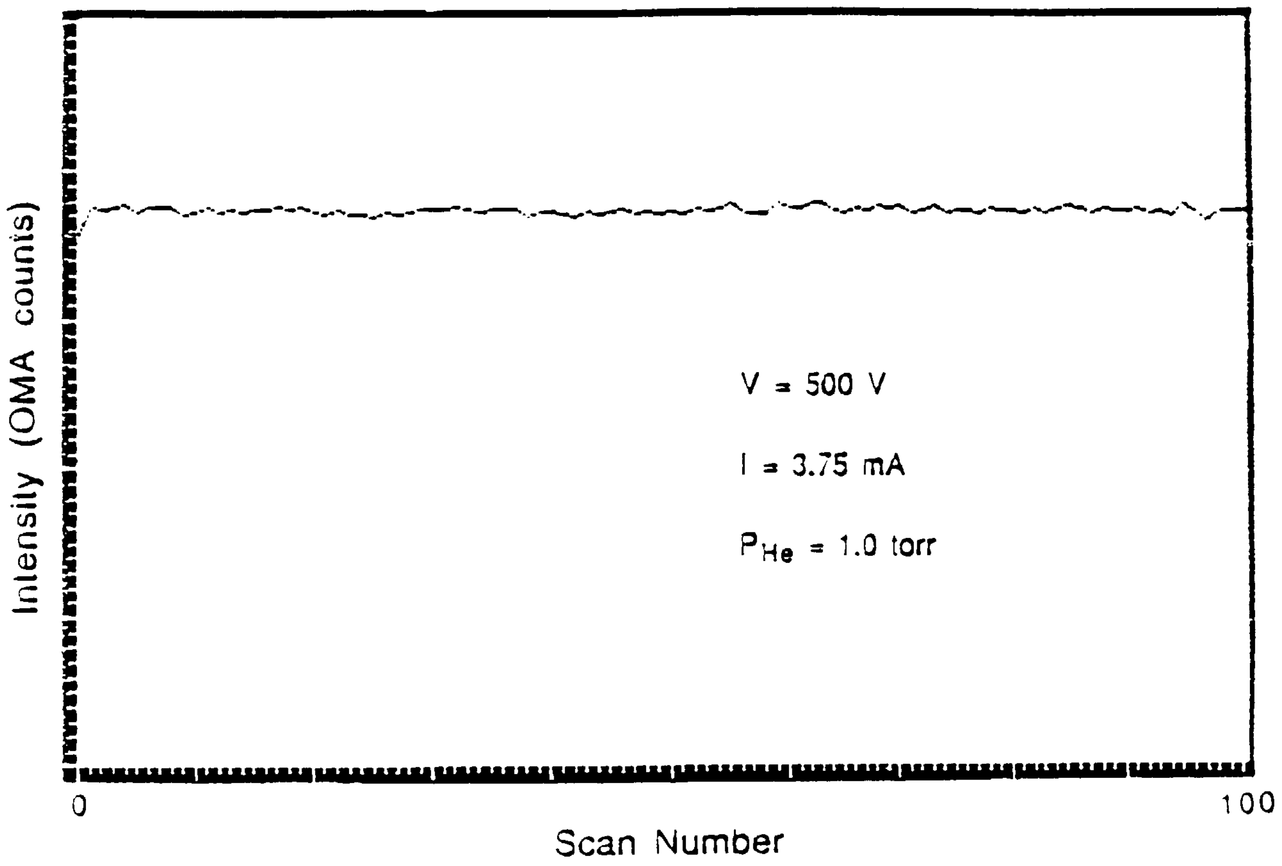

Figure 10. The stability of He* for 200 seconds under the same conditions as in figure 9.

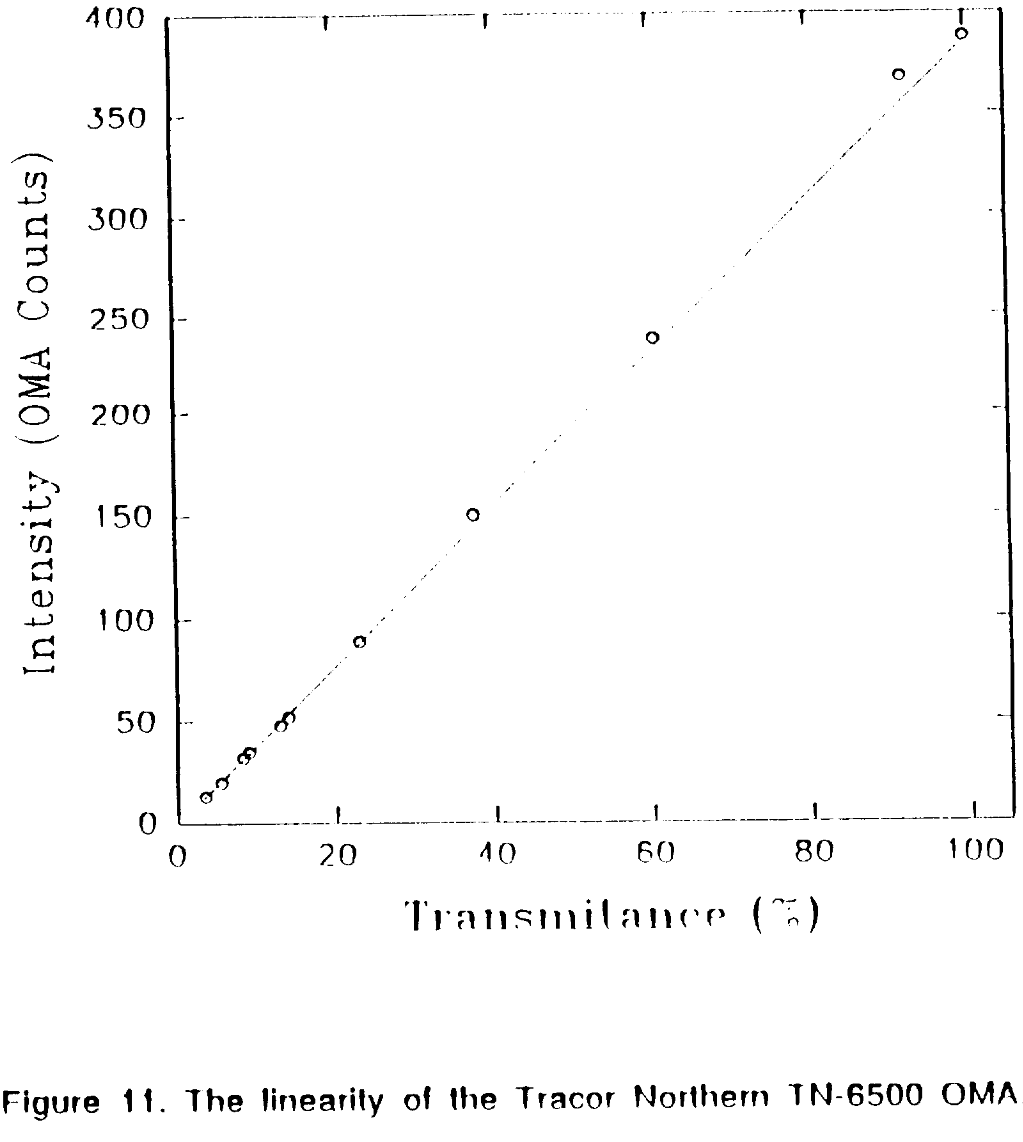

Figure 11. The linearity of the Tracor Northern TN-6500 OMA.

photomultiplier tube (PMT) was used for a high resolution. The grating used was blazed at 300 nm and had 3600 groove/mm which resulted in a linear dispersion of 0.55 nm/mm. The widths of entrance and exit slits were 20 mm and 10 mm, respectively, which resulted in a 0.02 nm of resolution. The Hamner N-4035 High Voltage Power Supply was used to bias thePMT at 2 kV. The output signal from the PMT was recorded with a X-T recorder (KIPP ZONEN model BD 111). For these measurements the monochromator had 10 nm/min of scanning speed, and the X-T recorder had a chart speed of 20 cm/min.

To determine the rotational and vibrational temperatures for the same sample, the optical axis of two systems were faced antiparallel to each other, and aligned by a He-Ne laser (Fig. 12). The beam of the He-Ne laser passed through the exit slit of monochromator went out to the center of the exit hole of the spectrometer which the OMA head has to be attached. The beam passed through the entrance slits of the monochromator and spectrometer when both were adjusted at the wavelength of He-Ne laser (632.8 nm).

4. RESULTS AND DISCUSSION

4-1. Error Analysis of Measurements

The measured data may contain some errors which inevitably occur during measurements. In the review of the experimental setup and the measurement procedures, three possible sources of errors could be introduced. The first error source resulted from the temporal fluctuations in the measured emission intensities due to the unsteady Penning ionization. To determine the effect of the fluctuations on the calculated rotational temperature, repeated scans over each of several spectral lines were made. The scanned results showed that the intensity fluctuation was about 10% in average for all lines. This intensity fluctuation introduced an error in the rotational temperature calculations from equation (7). The change was about ±1% for the temperature around 330 K.

The second source of error in the measured rotational temperature arises due to the neglect in the Boltzmann plot of the P-branch lines that overlap the R-branch lines. Since the rotational lines R(J") and P(J" + 27) are separated by only about 0.025 nm, it would be expected that the lines overlap. Two types of combination lines would result: the first is a combination of an

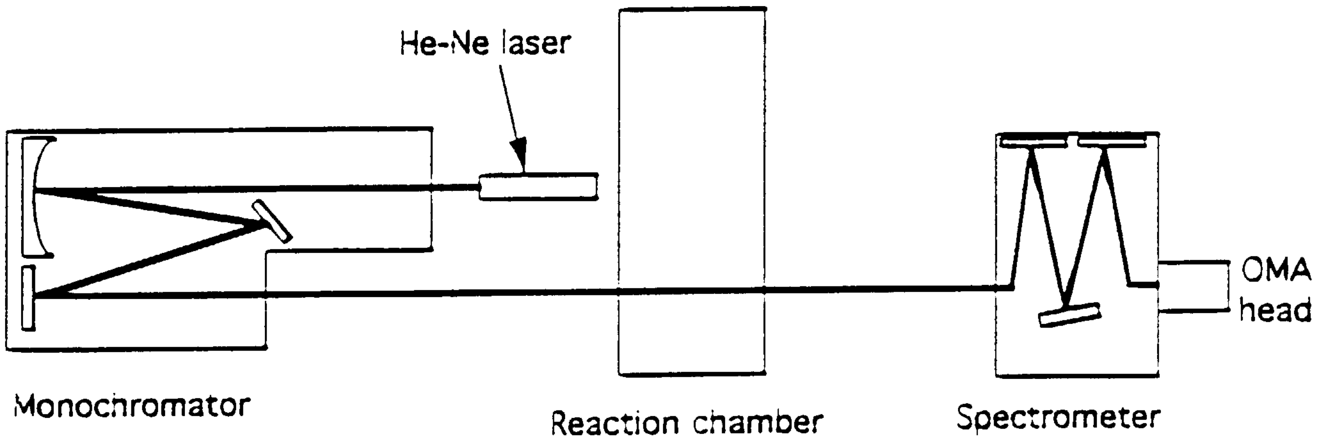

Figure 12. The alignment of the detection systems for detecting a same sample.

odd P-branch line and even R-branch line, and the second is with even P and odd R. The computer codes of Seitzman [30] showed that the P-branch lines were always weaker than their overlapping R-branch lines for the first type in the temperature range of less than 2000 K. Since the intent in performing the experiment was to minimize the contribution of nearby P-branch overlap, only the even R-branch lines were used for the data reduction. Then, in calculating the rotational temperature from the Boltzmann plot, only the R-branch lines were considered even though the P line were unresolved. According to Seitzman's study [30], the error is approximately ±5% for the temperature range between 3100 K and 4800 K. Therefore, the error in this experimental data for the temperature range from 300 K to 400 K will be less than 5% because the line intensity of a high rotational quantum number at a low temperature is weak.

The third source of error in the temperature measurement is due to line-of-sight averaging. This error turns out to be the most significant of the three experimental errors, but is the most difficult to quantify. This difficulty arises because the spatial variation of flowfield properties needs to be known in order to estimate the error. The signal for each rotational line depends on temperature and pressure. However the pressure varied by a factor of 2 to 3 across the flow on an axial location, the calculated temperature error due to the line-of-sight averaging were almost the same. The rotational line radiation is absorbed while travelling through the flowfield. The absorption of radiation is given by the Beer-Lambert law as

$$I/I_0 = \exp(-\alpha PL) \tag{18}$$

where I/I_0 is the ratio of transmitted to incident intensities, α is the absorption coefficient (cm^{-1} atm^{-1}), P is the partial pressure of the absorbing species (atm), and L is the path length (cm). The Cohen's result [31] showed that the absorption was never higher than 0.001%. Therefore the dominant factor affecting the error was clearly the variation of temperature across the flowfield. A prediction of such an error was obtained from the Method of Characteristics (MOD) code solution by Palmer [32], and the error appears at the 7 - 8% level. The MOD code has been used to model underexpanded jets. The only inputs that the code requires are the pressure ratio across the nozzle and the isentropic exponent.

An overall experimental error bar was obtained by calculating the square root of the sum of the squares of the individual values. It was assumed that the individual sources of error are not related to each other. The resulting overall error was about ±9.5%.

4-2. Absolute Intensity Calibration Factors

For the determination of the vibrational temperature from emission spectra, the signal strength was measured over a relatively large wavelength region between 328.35 nm and 480.18 nm (Fig.13). Because of the different responsivity of the optical detection system and the different transmittance of the Plexiglas for the 391.44 nm (0-0) and 358.21 nm (1-0) lines of N_2^+, the detector signal has to be calibrated for each emission lines.

The calibrated irradiance, I_l, will be

$$I_l = l\alpha\beta NC(\lambda) \tag{19}$$

where l is the linearity correction factor, α is the distance correction factor, β is the transmittance correction factor, N is the number of OMA counts, and $C(\lambda)$ is the absolute intensity per count at a wavelength l. The linearity correction factor, I, was unity (see Fig.11). The distance correction factor, a, was determined by measuring the relative intensity along the distance between the detection system and standard light source. The result is shown in figure 14. The intensity was inversely proportional to r^2 with less than 1% of error when the distance is more than 45 cm apart for both lines. For the 40 cm of distance, the error was 9%. Because all data of this experiment were obtained at the distance of 47 cm, the a was 0.8836.

The transmittance correction factors, b, were determined by comparing the intensities with and without Plexiglas at each wavelength (Fig.15). The measured transmittance were 0.453 and 0.859 at 358.21 nm and 391.44 nm respectively. Therefore the correction factors β's were 2.201 and 1.164, respectively, because the β's are the inverse of the transmittances.

The absolute intensity per count (Fig.16) was measured by using the EG & G GS-900 standard light source at 50 cm of the distance which is set by the company. The results were 1.522×10^{-10} W/cm^2 nm for the (1-0) line and 1.838×10^{-10} W/cm^2 nm for the (0-0) line. The summary of the intensity calibration is shown in table 4. The calibrated irradiance was determined by multiplying the measured counts, N, by the calibrated irradiance per count, $C'(\lambda) = l\alpha\beta C(\lambda)$.

4-3. Radiative Properties of the Reactions.

Figure 17 shows the irradiance of the N_2^+, B-X (0,0) bandhead as a

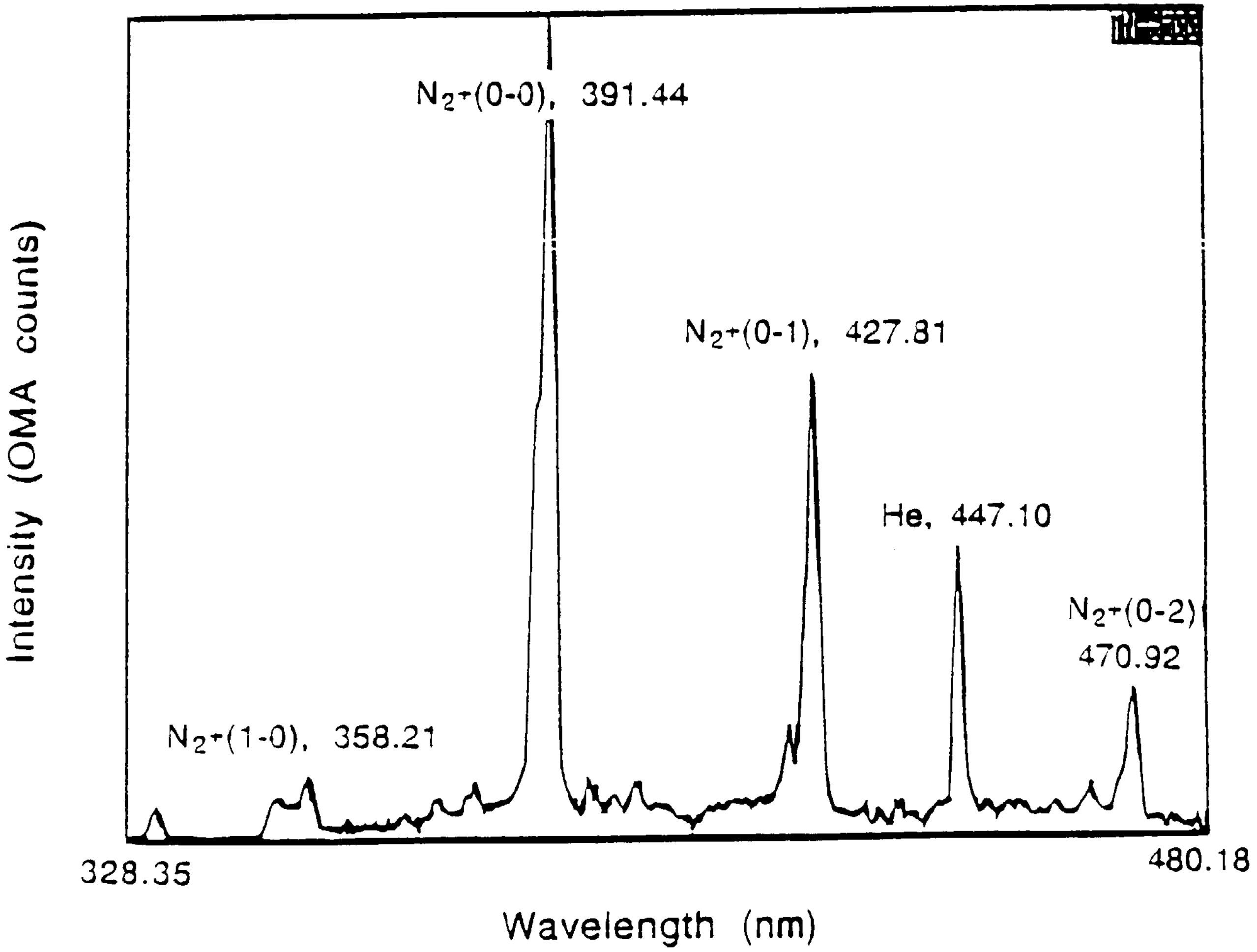

Figure 13. The measured spectrum by TN-6500 OMA to calculate the vibrational temperature.

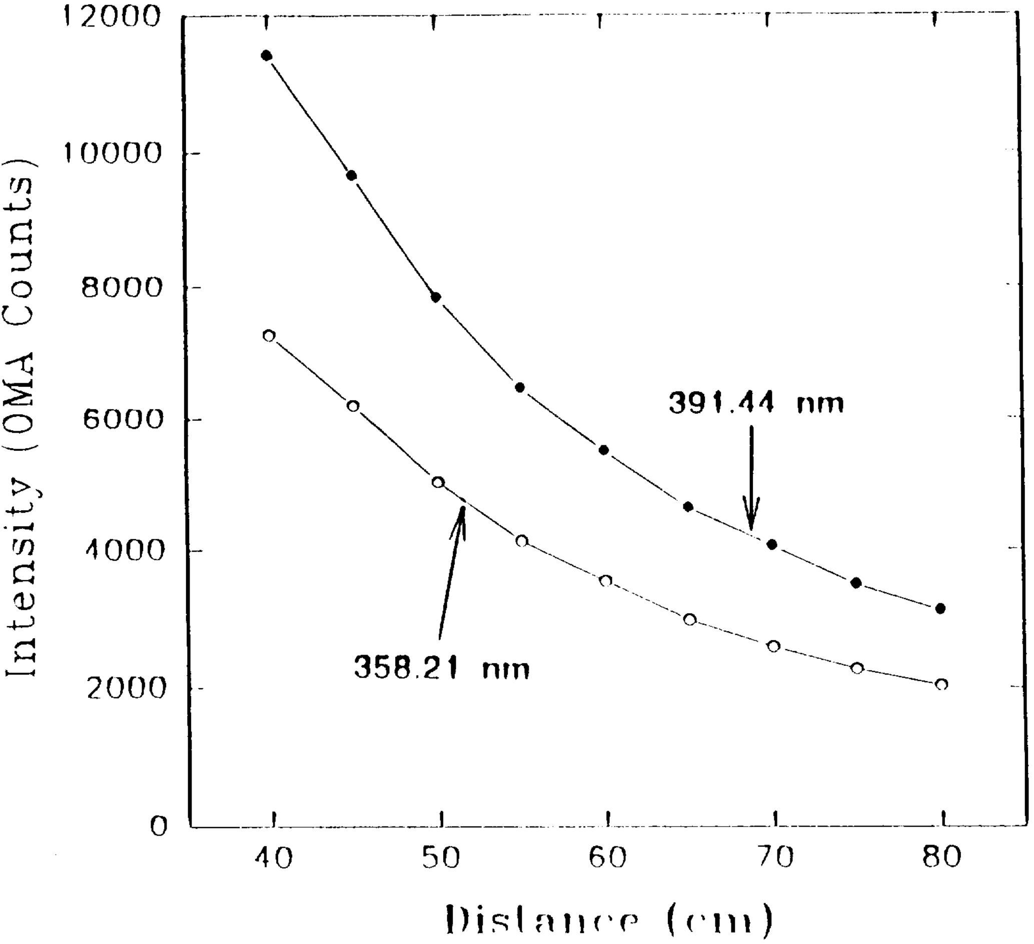

Figure 14. The measured relative intensity by changing the distance between the optical detection system and the standard light source to define the distance correction factors.

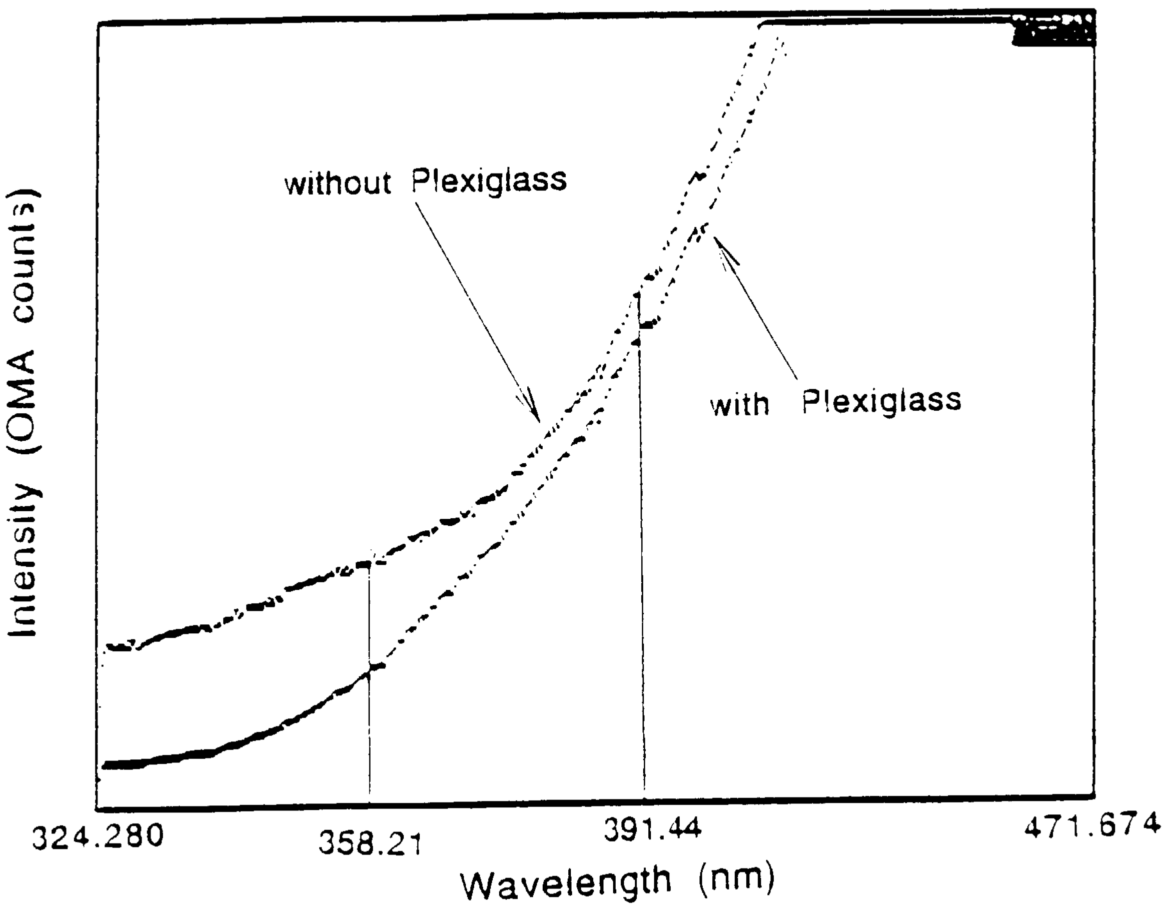

Figure 15. The measurement for the transmittance correction factor.

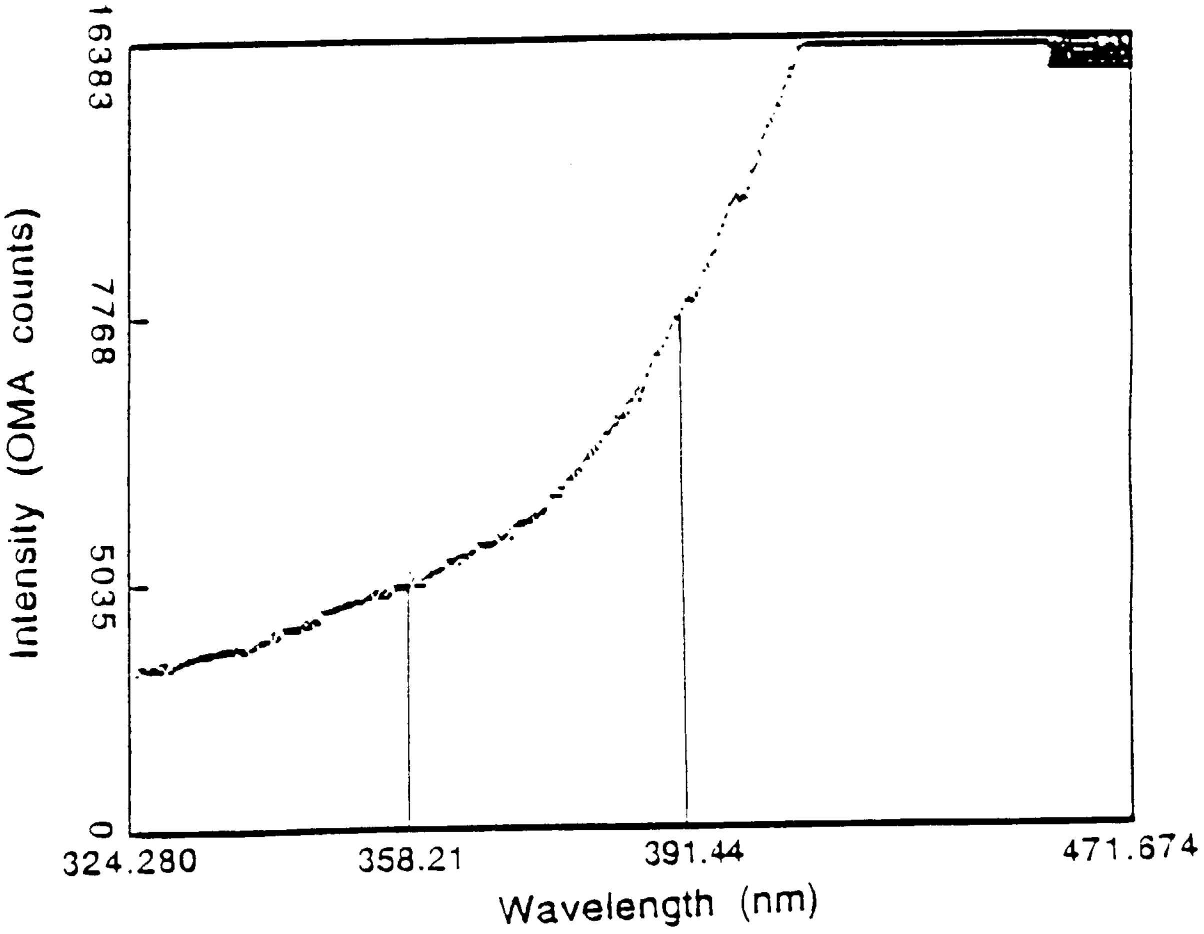

Figure16. The measurement for the irradiance per count.

function of the discharge current. The irradiance was linearly proportional to the current in the range from 2 to 5.25 mA because higher current produces more number density of He^*. The current was varied with the current limiting resistor connected to the power supply output at a fixed voltage (500 V). The helium pressure was fixed at 1.0 torr, and the nitrogen flowrate was 30 SCCM.

Figure 18 shows the irradiance of the N_2^+, B-X (0-0) line as a function of the helium pressure at the conditions of 500 V of discharge voltage, 30 SCCM of nitrogen flowrate, and 3.75 mA of current. The irradiance increases with the increase of the number density of helium. At a high pressure range (> 2.0 torr), the irradiance fluctuated because the vacuum pump could not maintain the constant pressure.

The irradiance dependence of the nitrogen flowrate is shown in figure 19. The conditions set for these measurements were 3.75 mA of current, 500 V of voltage, and 1.0 torr of helium pressure. Under these conditions, the irradiance had an incremental trend with the increase of N_2 flowrate up to 50 SCCM, and saturated after that point. The saturation may be caused by collisional quenching of the excited molecular nitrogen ions with the molecular nitrogen at high concentrations. From these three preliminary results (Fig. 17, 18, and 19), the experimental conditions for remaining tests were fixed at 500 V of discharge voltage, 3.75 mA of current, 1.0 torr of helium pressure, and 30 SCCM of nitrogen flowrate to ensure a relatively high irradiance with a small signal fluctuation.

Figure 20 shows the irradiance profile along the axial distance from the nitrogen injector. The hollow-cathode discharge side is designated as negative positions, and the vacuum pump side as positive positions. Most of the collisions between He^* and N_2 occurred within ±2 mm region away from the injector. The radiances at the negative positions were almost the same over the range from -15 mm to -3 mm because the diffused nitrogen gas was stagnated with a uniform number density at this region. The irradiances in the positive region were observed as decreased exponentially along the distance from the injector. The reason is that the number densities of nitrogen and He^* decrease as a function of distance in this region as the gases diffuse into a larger volume. Figure 21 and 22 show the irradiances versus the content of argon and CO_2. When argon or CO_2 gases were added, the number density of N_2^+ could be reduced by the reaction (12) and (14). With the 50% of argon mixture, the emission was reduced by about 34%. In the case of CO_2, it was reduced about 78% at the same mixing ratio. This results indicate that a high quenching rate of molecular nitrogen ions and excited molecular nitrogen ions with argon and CO_2 exists. The quenching effect by

	(0-0) line	(1-0) line
Linearity correction factor	1	1
Distance correction factor	0.8836	0.8836
Transmittance correction factor	1.164	2.201
Irradiance per count ($W/cm^2 nm$) $\times 10^{10}$	1.838	1.522
Calibrated irradiance per count ($W/cm^2 nm$) $\times 10^{10}$	1.89	2.96

Table 4. The summary of the correction factors and calibrated irradiance.

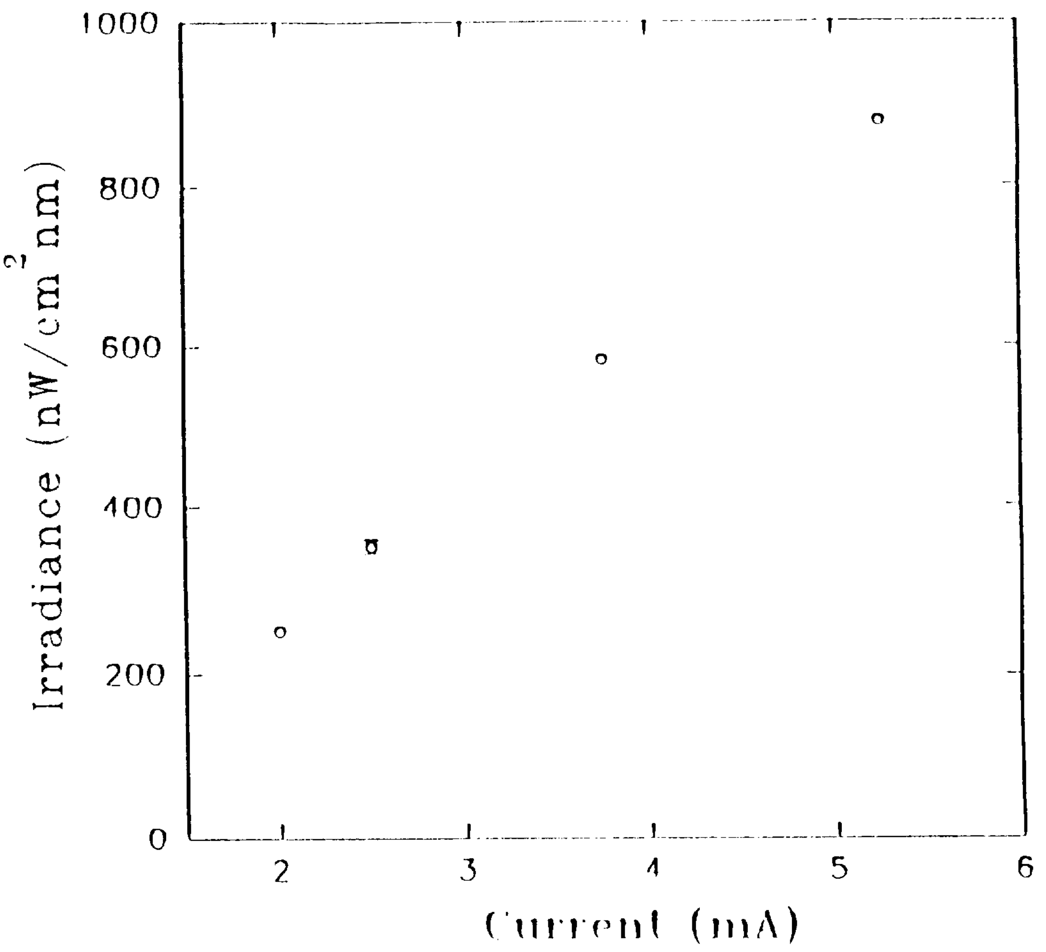

Figure 17. The irradiance of the N_2^+, B-X(0-0) bandhead versus the discharge current.

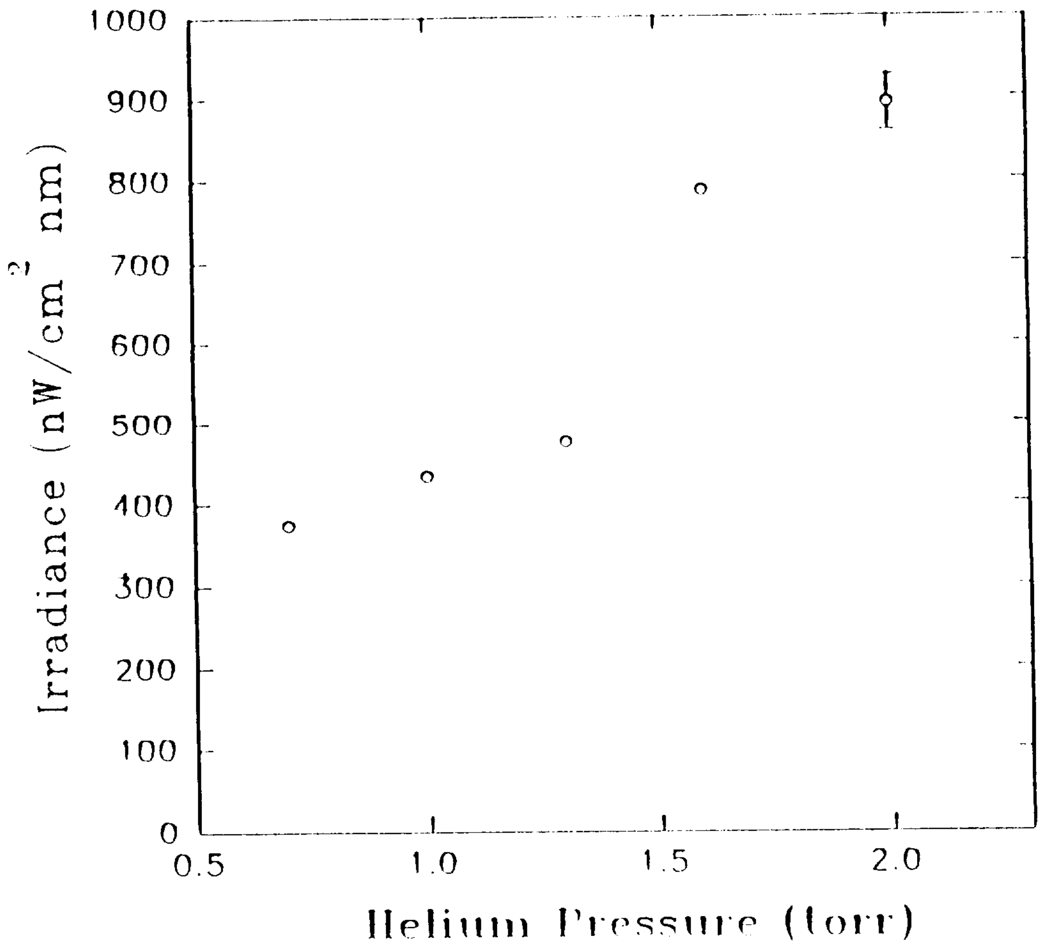

Figure 18. The irradiance of the N_2^+, B-X(0-0) bandhead versus the helium pressure.

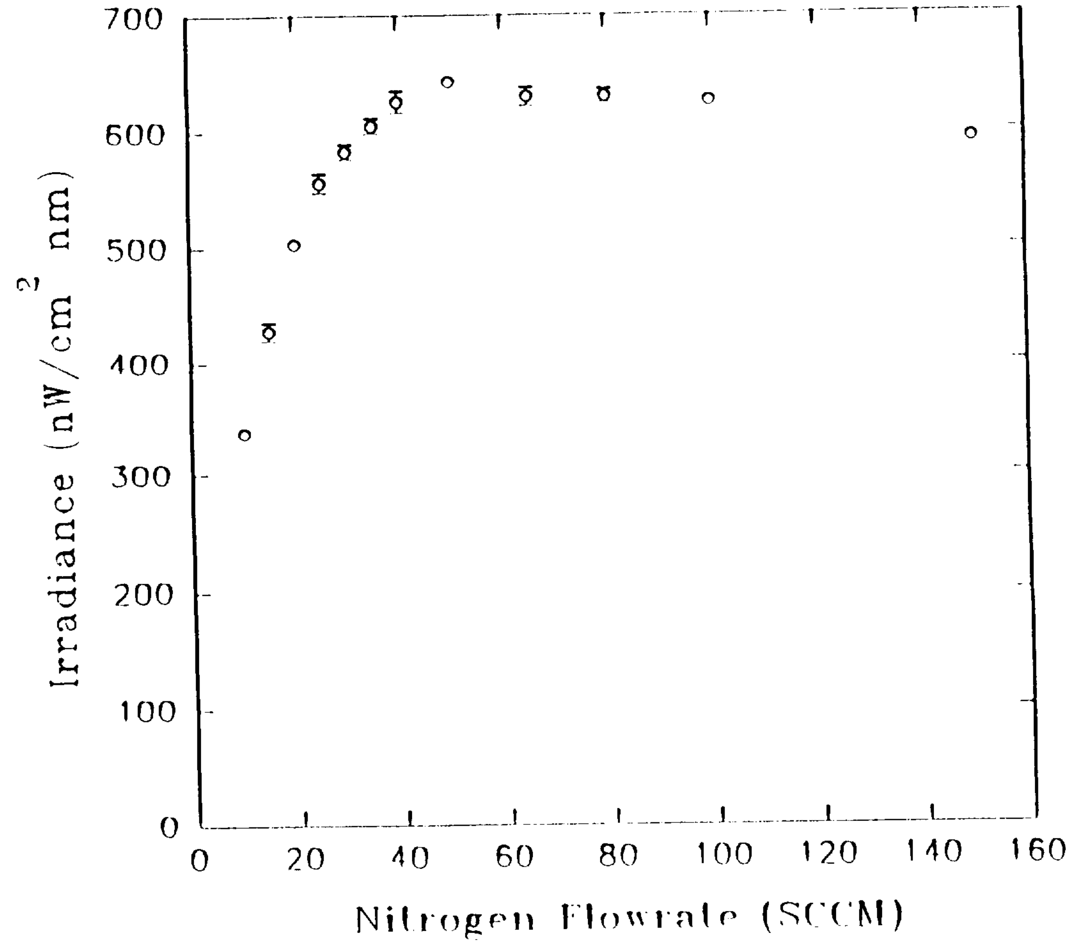

Figure 19. The irradiance of the N_2^+, B-X(0-0) bandhead versus the nitrogen flowrate.

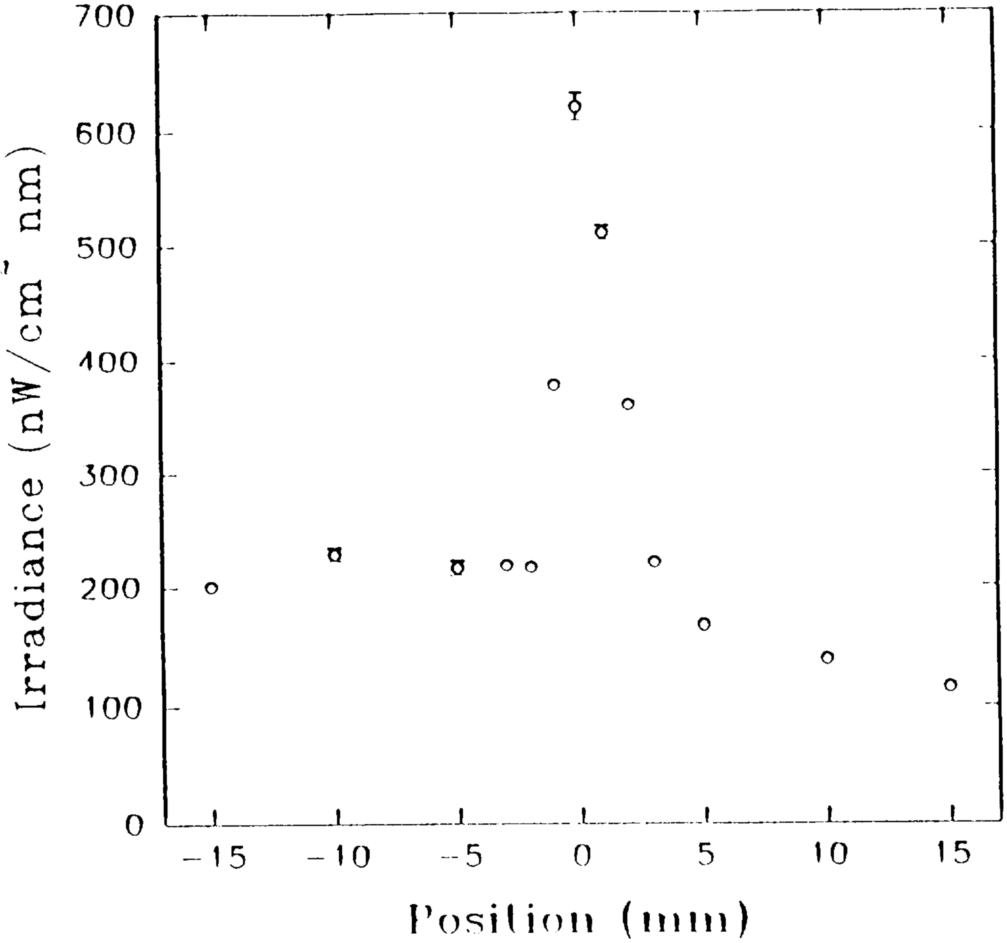

Figure 20. The irradiance of the N_2^+, B-X(0-0) bandhead versus the position.

CO_2 was more remarkable because of its larger molecular diameter (0.459 nm) than that of argon (0.375 nm). However the effects by a small amount of Ar or CO_2 in the mixture was insignificant. This result leads to a conclusion that the effects of argon and CO_2 at the upper atmosphere flight region where the 0.9% of argon and the 0.03% of CO_2 exist are not significant as speculated.

4-4. Rotational Temperature.

The rotational temperatures were calculated by the Boltzmann plot (equation 7). Figure 23 presents an emission spectrum of the N_2^+, B-X (0,0) band and helium atomic line at 388.91 nm under the conditions of 500 V of discharge voltage, 3.75 mA of current, 1.0 torr of helium pressure, and 30 SCCM of nitrogen flowrate. The intensities of each rotational line and rotational quantum number of transitions are shown in table 5. A rotational temperature was estimated by the use of relative rotational line intensities, I, by plotting the logarithm of the quantity $I_{J'J''}/(J' + J'' + 1)$ versus $J''(J'' + 1)$ as shown in figure 24. The plot yields a straight line for a Boltzmann distribution whose slope is proportional to $-1/kT_R$. A least squares fit to the data in figure 23 yields a rotational temperature, $T_R = 339.4$ K. All rotational temperatures were calculated by the same method. Figures 25, 26, 27, 28, 29 and 30 show the rotational temperatures versus current, helium pressure, nitrogen flowrate, position, argon content, and CO_2 content respectively. The temperatures did not change in all cases. The error bars were obtained from the Section 4-1.

4-5 Vibrational Temperature.

The vibrational temperatures were calculated from the equation (5) by measuring the absolute intensities of N_2^+ ,B-X (0,0) and (1-0) lines. The vibrational temperature was not remarkably varied by the input current (Fig. 31), the helium pressure (Fig. 32), the nitrogen flowrate (Fig. 33), and the position (Fig. 34) changes.

When argon gas was added, the vibrational temperature was increased as shown in figure 35. At the 33.3% of argon mixture, the vibrational temperature was increased by 9.8%. These results agree with the result of Schonemann [33]. The vibrational temperature was increased by 24.1% for the 50% of argon mixture. With the 50% of CO_2 mixture (Fig. 36), the vibrational temperature was increased by 82.9%. From this trend we can conclude that

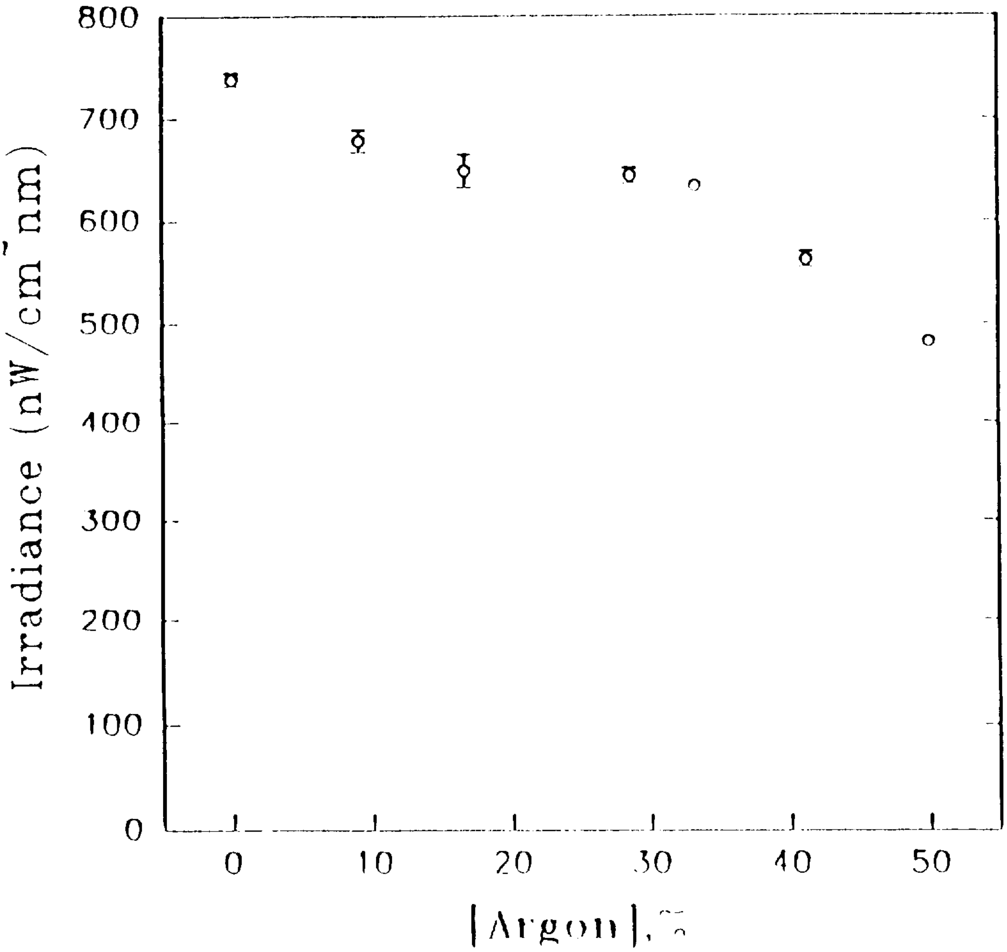

Figure 21. The irradiance of the N_2^+, B-X(0-0) bandhead versus the content of argon.

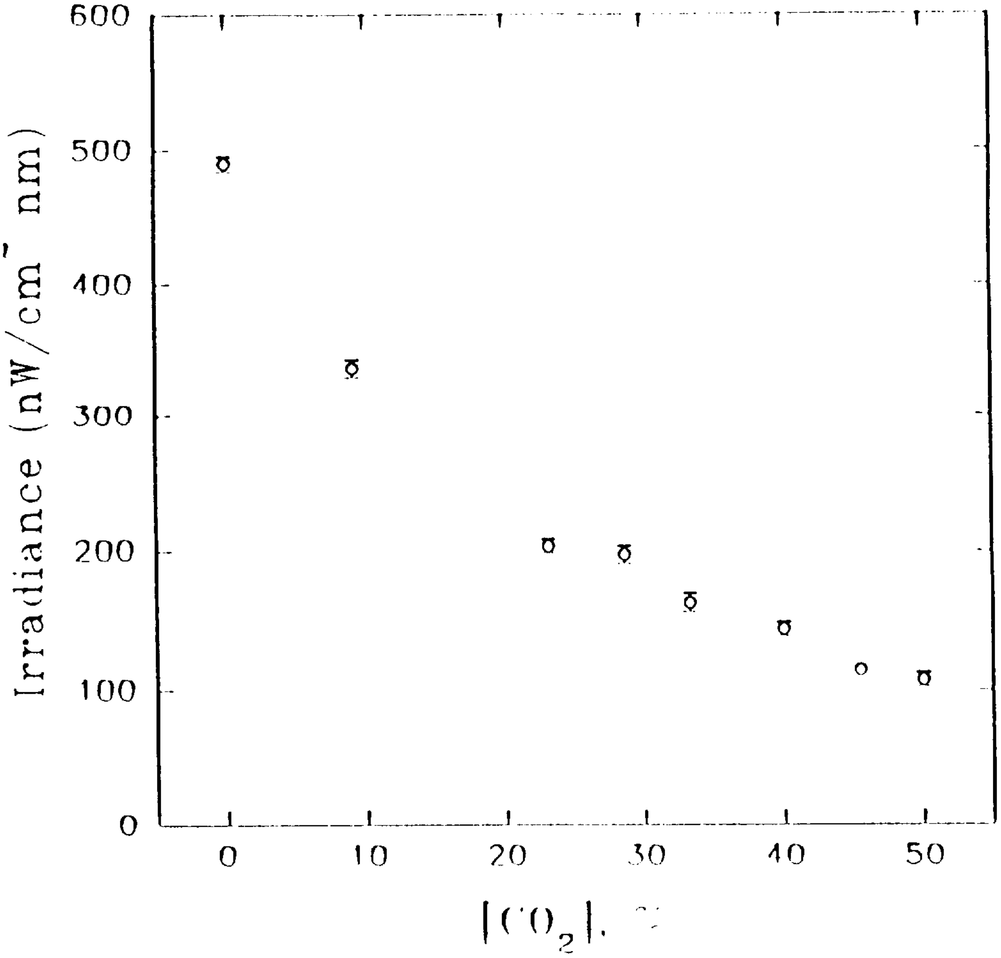

Figure 22. The irradiance of the N_2^+, B-X(0-0) bandhead versus the content of CO_2.

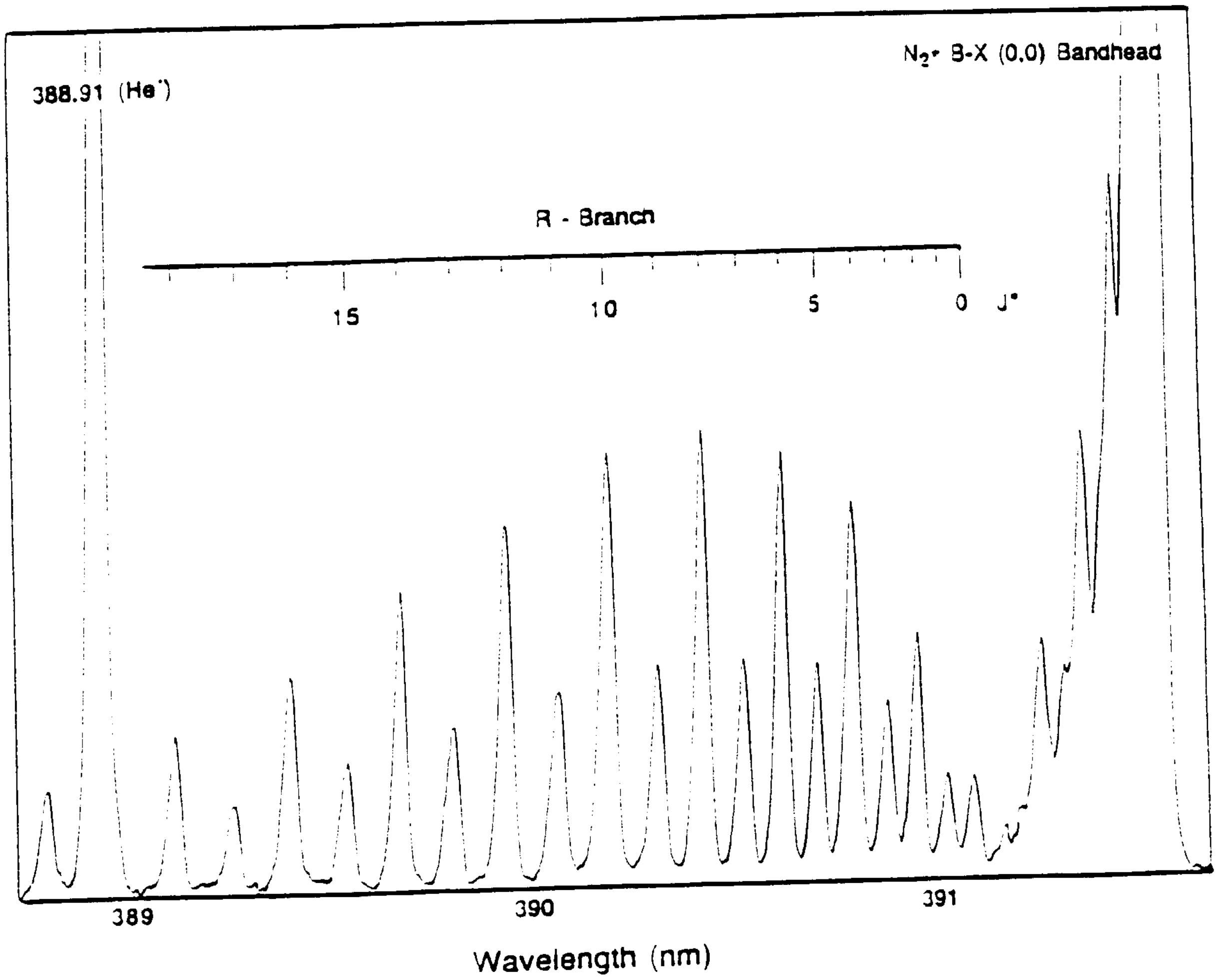

Figure 23. The rotational spectra of the first negative bandhead of N_2^+.

J'	1	3	5	7	9	11	13	15	17	19
J"	0	2	4	6	8	10	12	14	16	18
J"(J"+1)	0	6	20	42	72	110	156	210	272	342
J'+ J"+ 1	2	6	10	14	18	22	26	30	34	38
Intensity (arb.)	16	37.5	58.5	66.5	70	66.5	56	45.5	33.5	25
ln[I/(J'+J"+1)]	0.903	0.796	0.767	0.677	0.590	0.480	0.333	0.181	-0.006	-0.182

Table 5. The rotational branch of the first negative bandhead of molecular nitrogen ion.

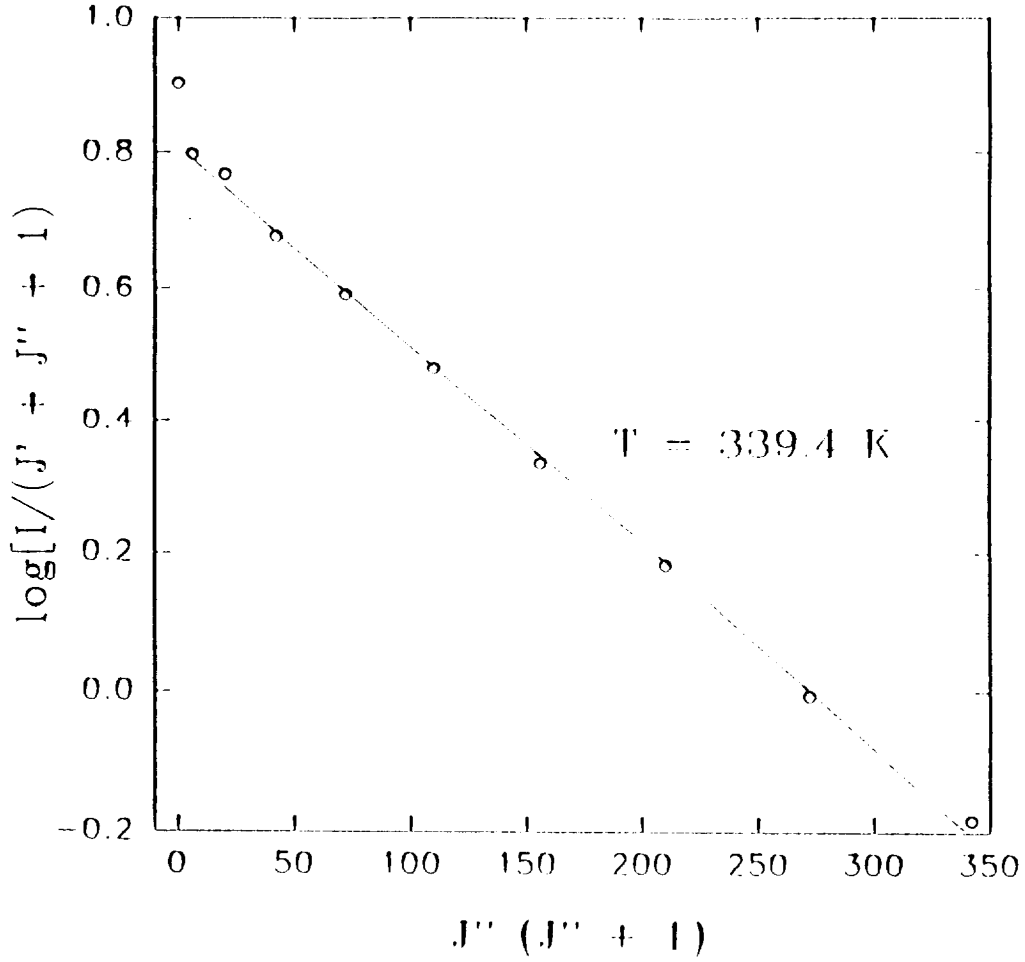

Figure 24. The least squares fit of even J' lines to calculate a rotational temperature.

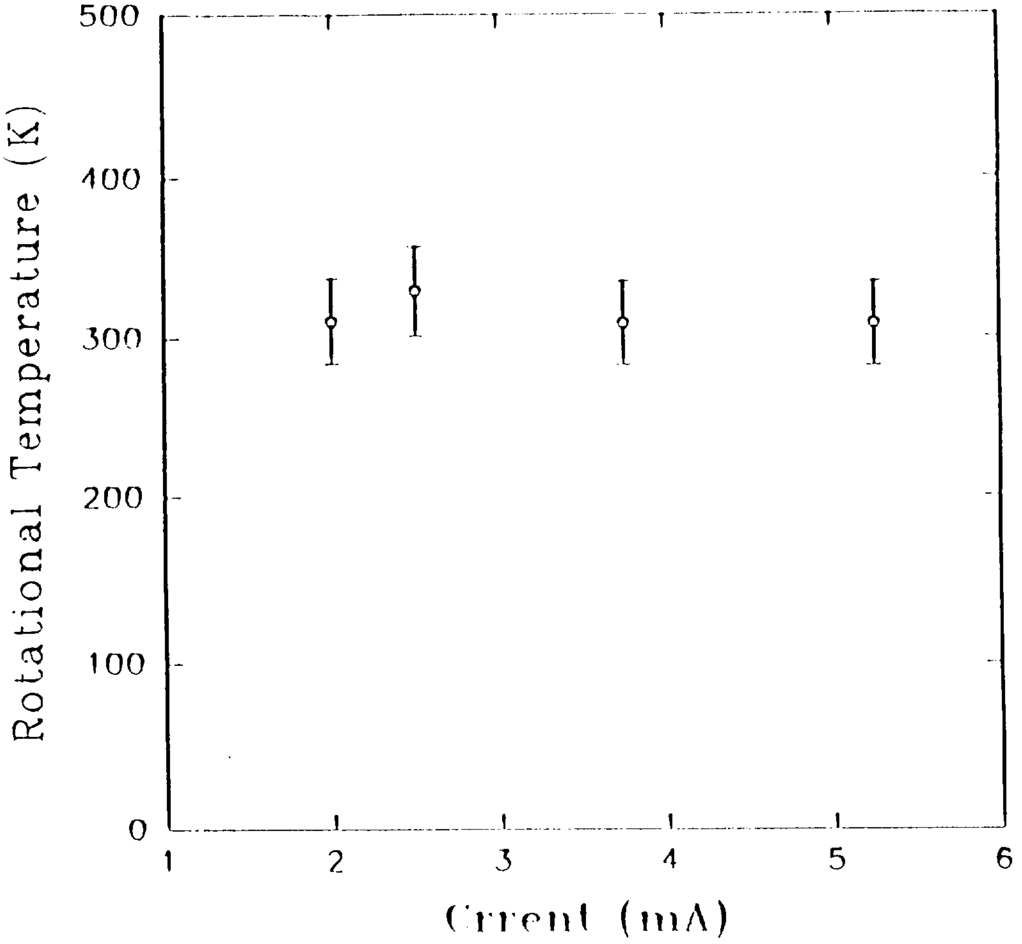

Figure 25. The rotational temperature versus the discharge current.

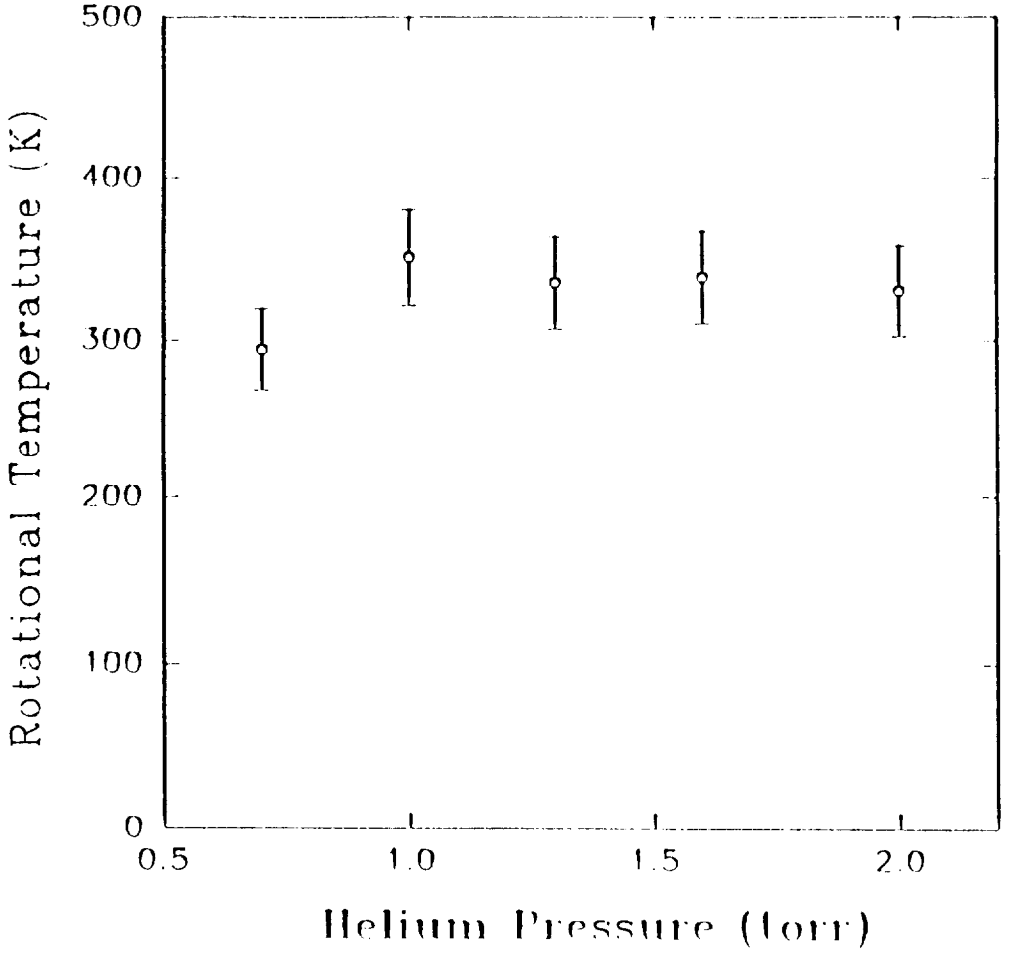

Figure 26. The rotational temperature versus the helium pressure.

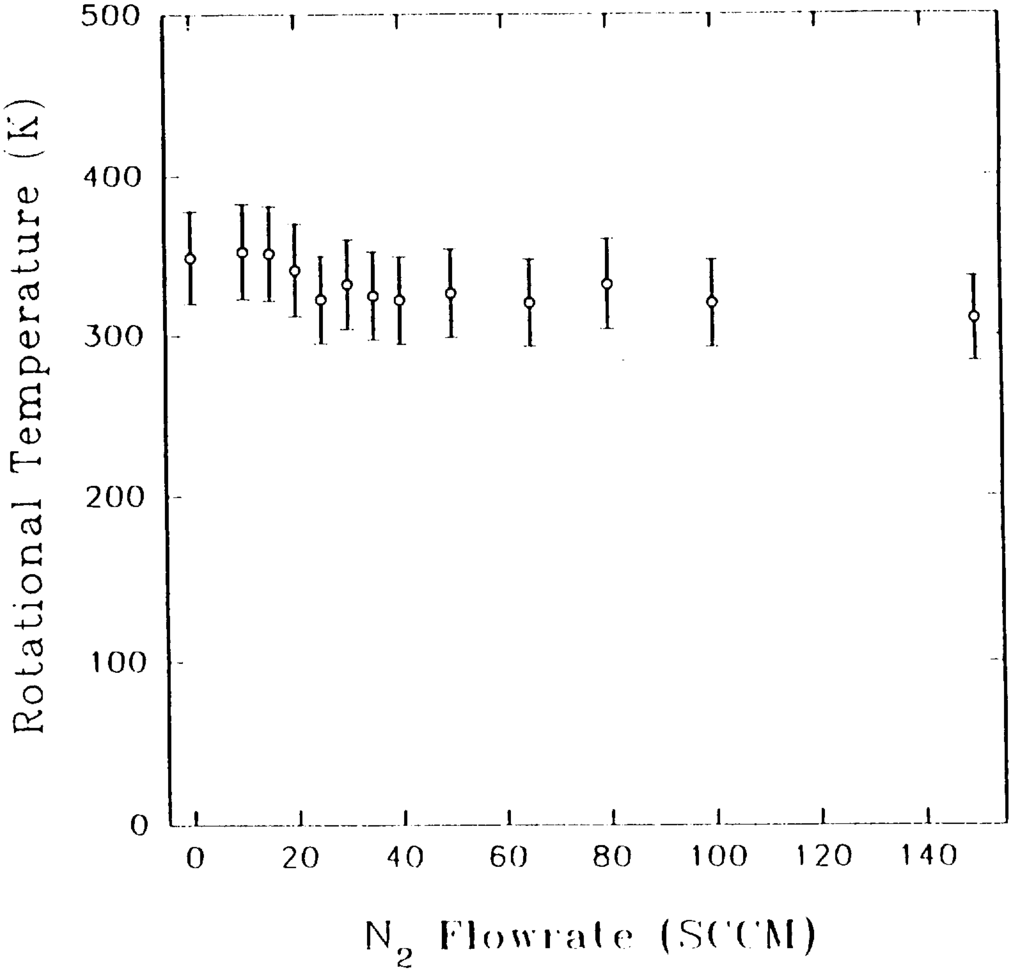

Figure 27. The rotational temperature versus the nitrogen flowrate.

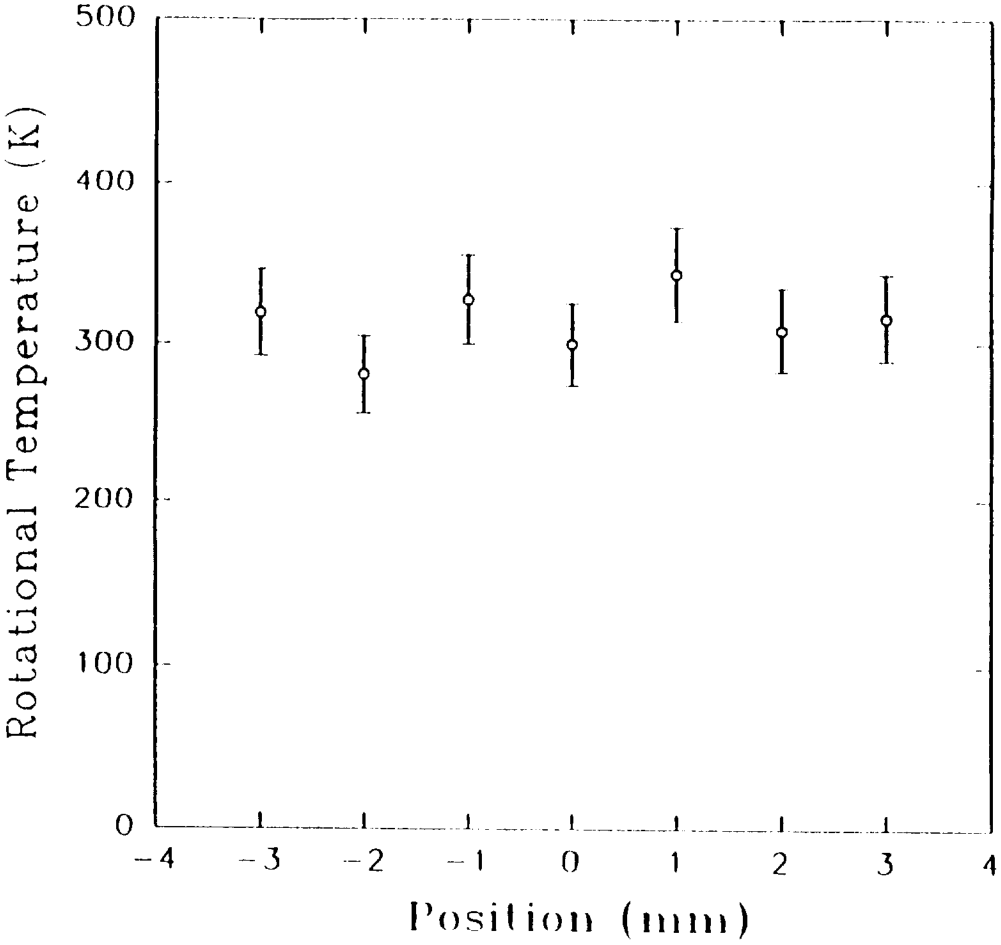

Figure 28. The rotational temperature versus the position

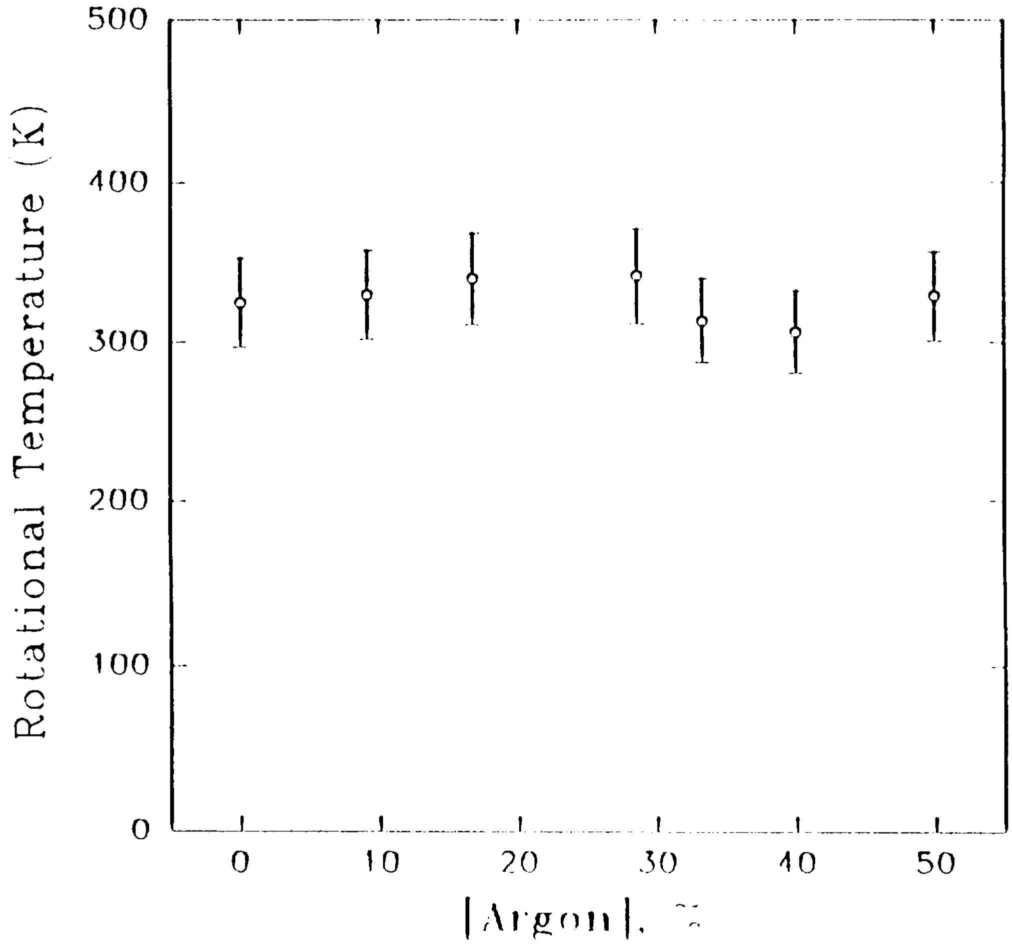

Figure 29. The rotational temperature versus the content of argon.

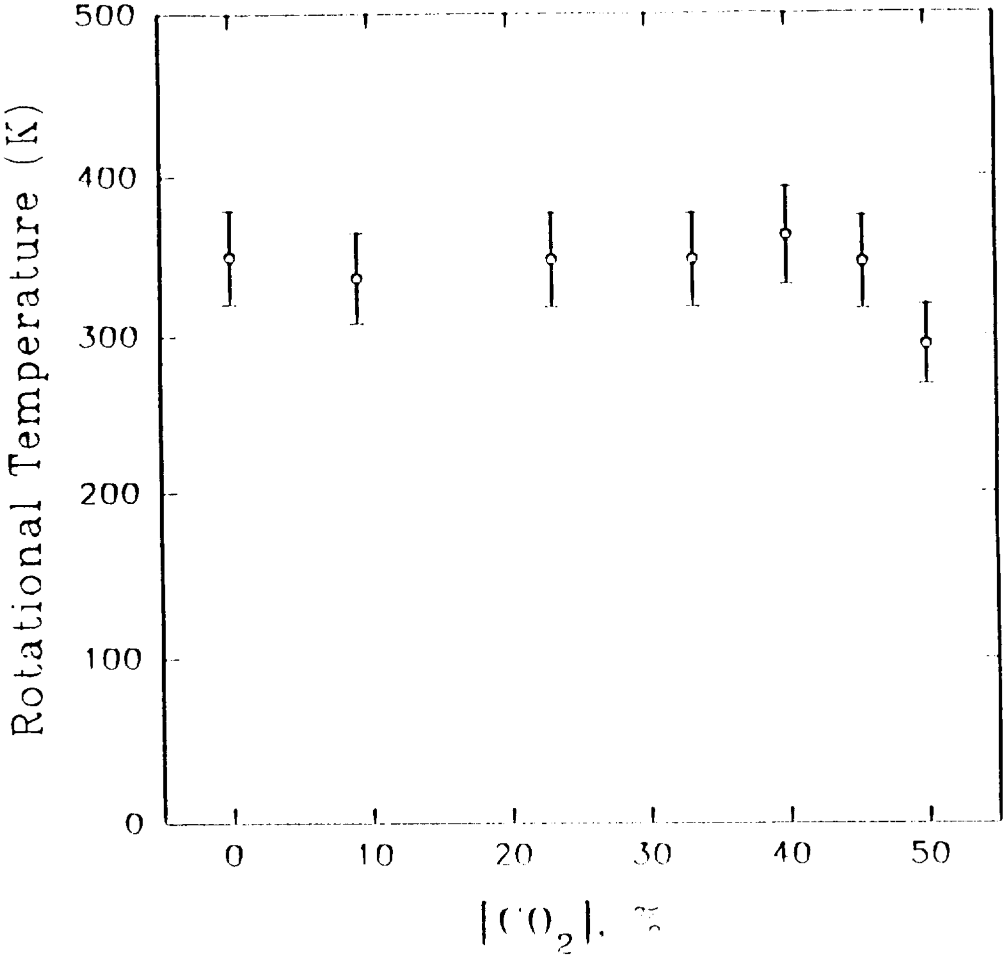

Figure 30. The rotational temperature versus the content of CO$_2$.

the effects of argon and CO_2 on the vibrational temperature of N_2^+ in the shock layer at the upper atmosphere flight region may be negligible for their small concentrations (< 1%).

4-6. Nonequilibrium Rotational and Vibrational Temperature

Because the distribution of energy among the rotational and vibrational modes in this experiment could not be described by a single temperature, the experimental conditions are clearly in thermal nonequilibrium. Nonequilibrium processes occur in a flow when the time required for a process to accommodate itself to local conditions within some region is of the same order as the transit time across the region. If the accommodation time is very short compared with the transit time, the medium is in equilibrium.

In this experiment, the vibrational temperature (18,000 - 36,000 K) was much higher than the rotational (300 - 370 K). These results disagree with the model used by the CFD codes for simulating hypersonic shock layers which assume a higher rotational temperature than the vibrational. However our Penning ionization result agrees with the experimental results of shock layers by Blackwell [18,19] and Sharma [20] as alluded earlier in Chapter 1. Also the rotational and vibrational temperature measurements of N_2^+ produced in the dayglow by photoionization showed higher vibrational temperature (6,000 - 8,000 K) than rotational (3000 K) [34].

Such nonequilibrium was also revealed in that, with the argon or CO_2 mixture, the vibrational temperature alone was increased while the rotational temperature remained constant indicating vibrational energy is exchanged with the translational energy through the inelastic collision of heavy particles which does not change the rotational temperature of the molecule. [35]

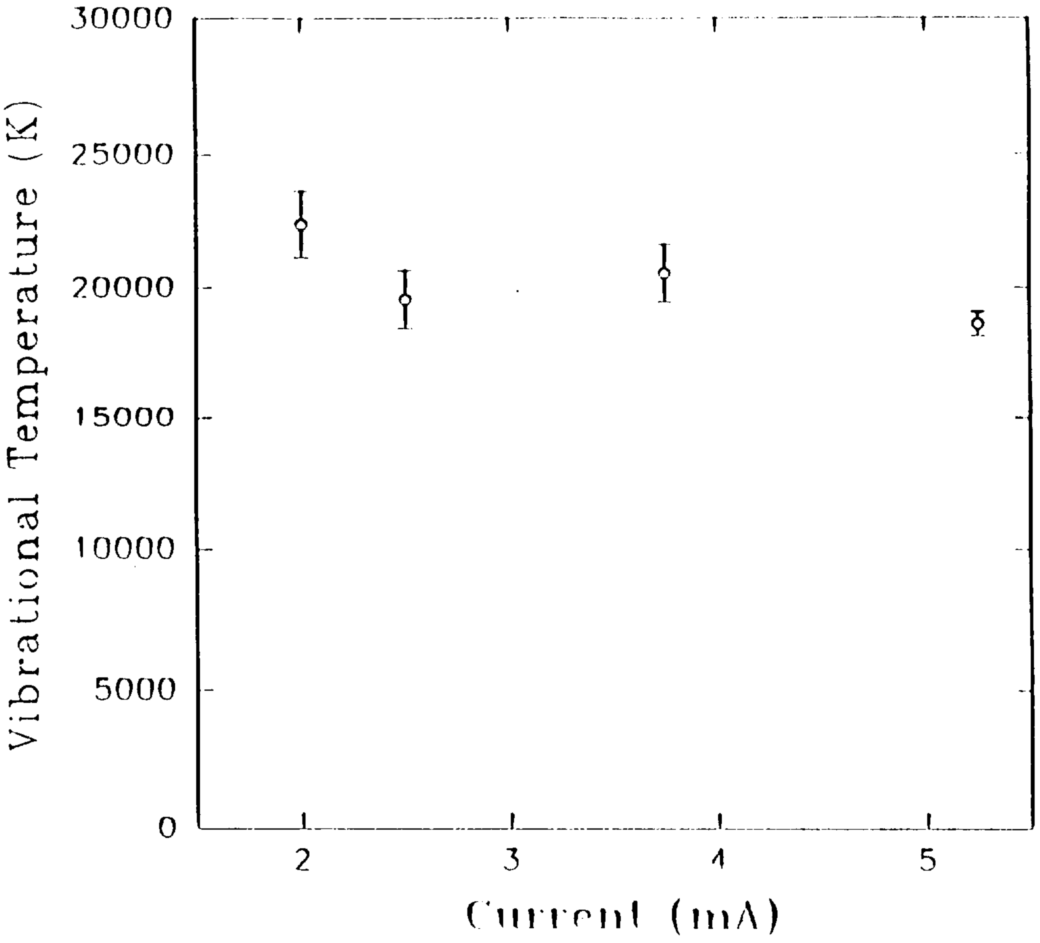

Figure 31. The vibrational temperature versus the discharge current.

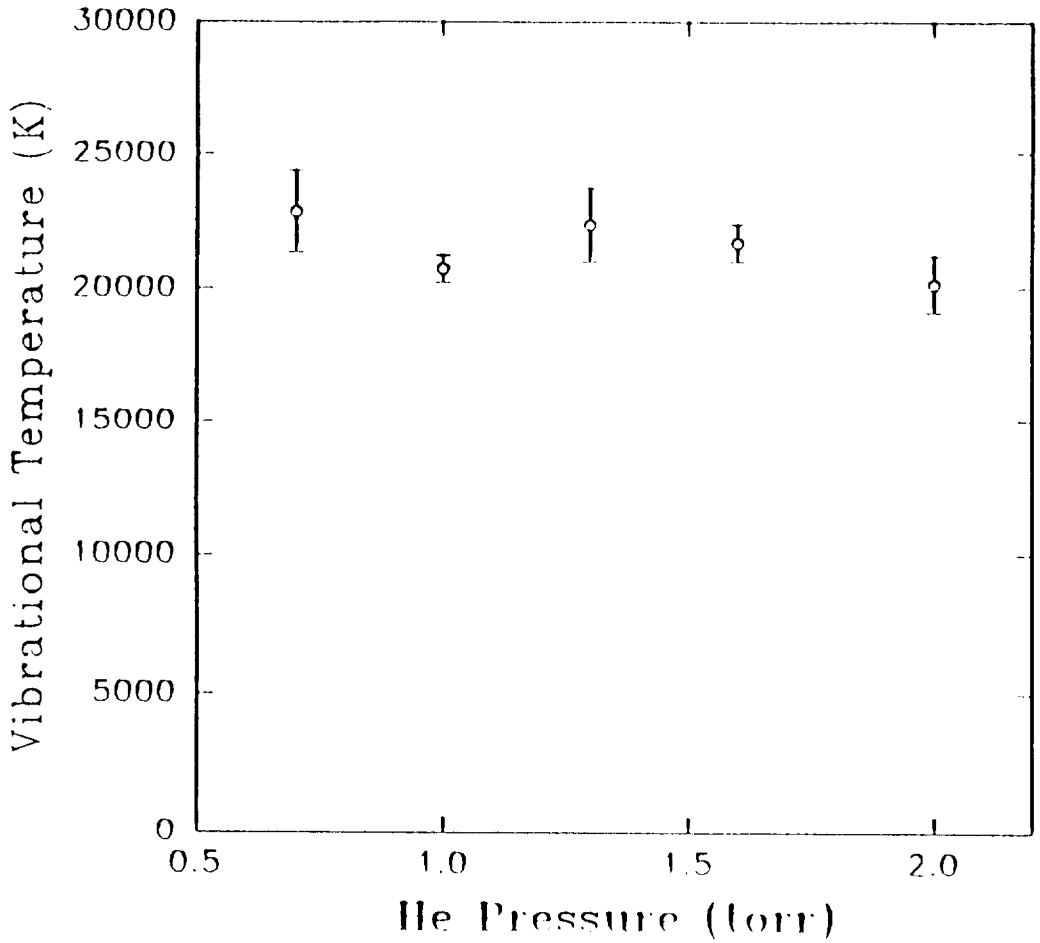

Figure 32. The vibrational temperature versus the helium pressure.

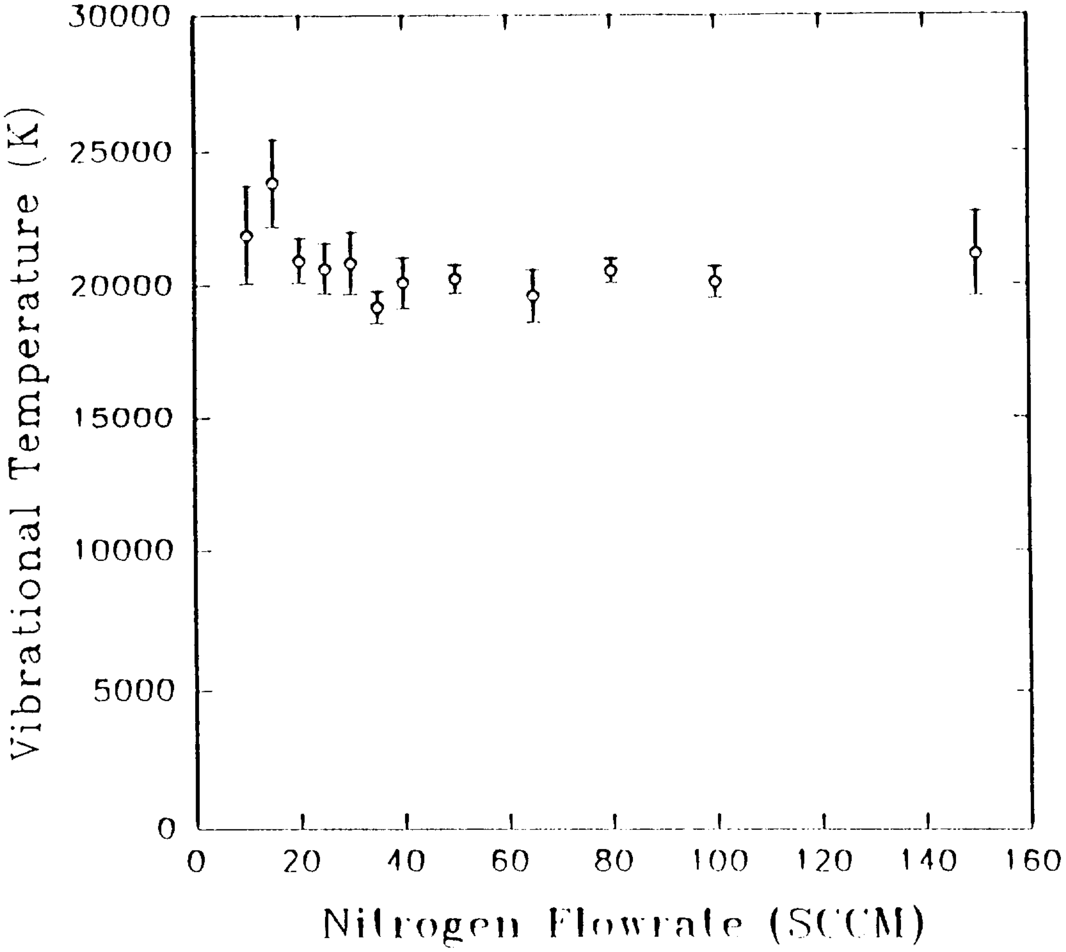

Figure 33. The vibrational temperature versus the nitrogen flowrate.

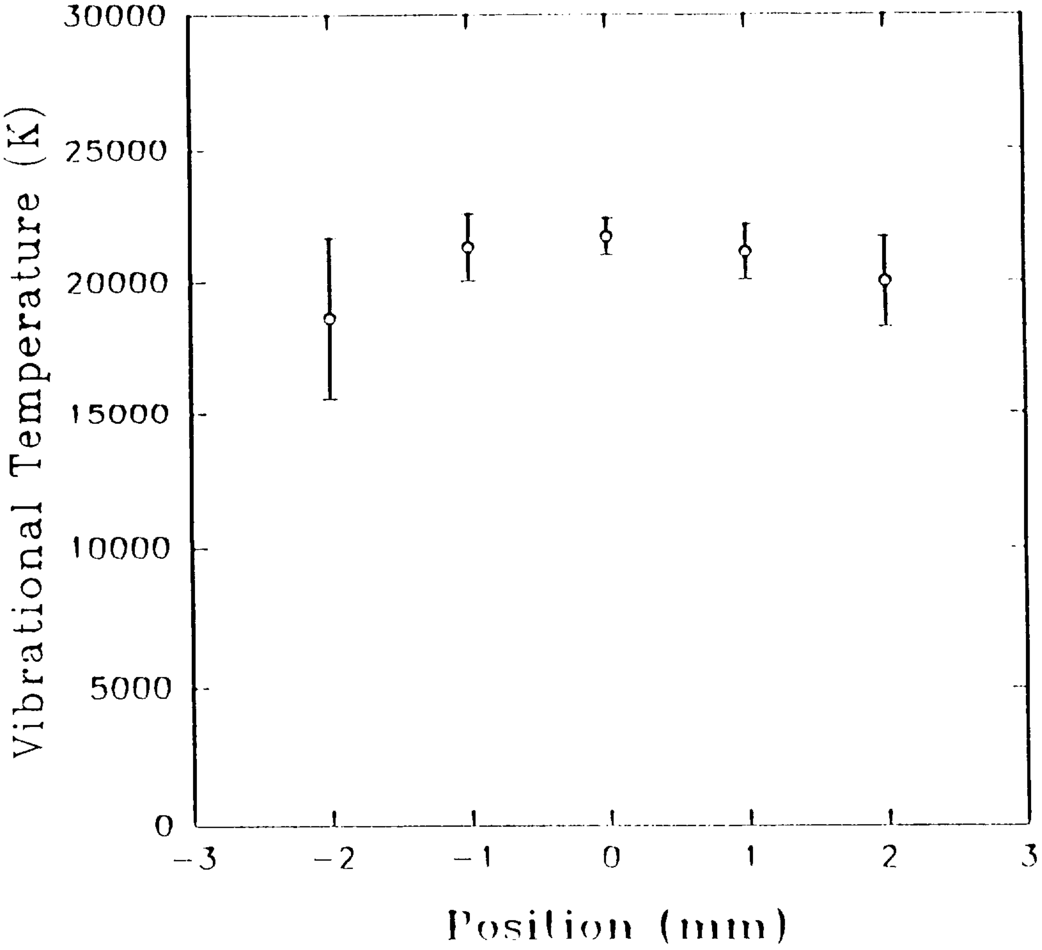

Figure 34. The vibrational temperature versus the position.

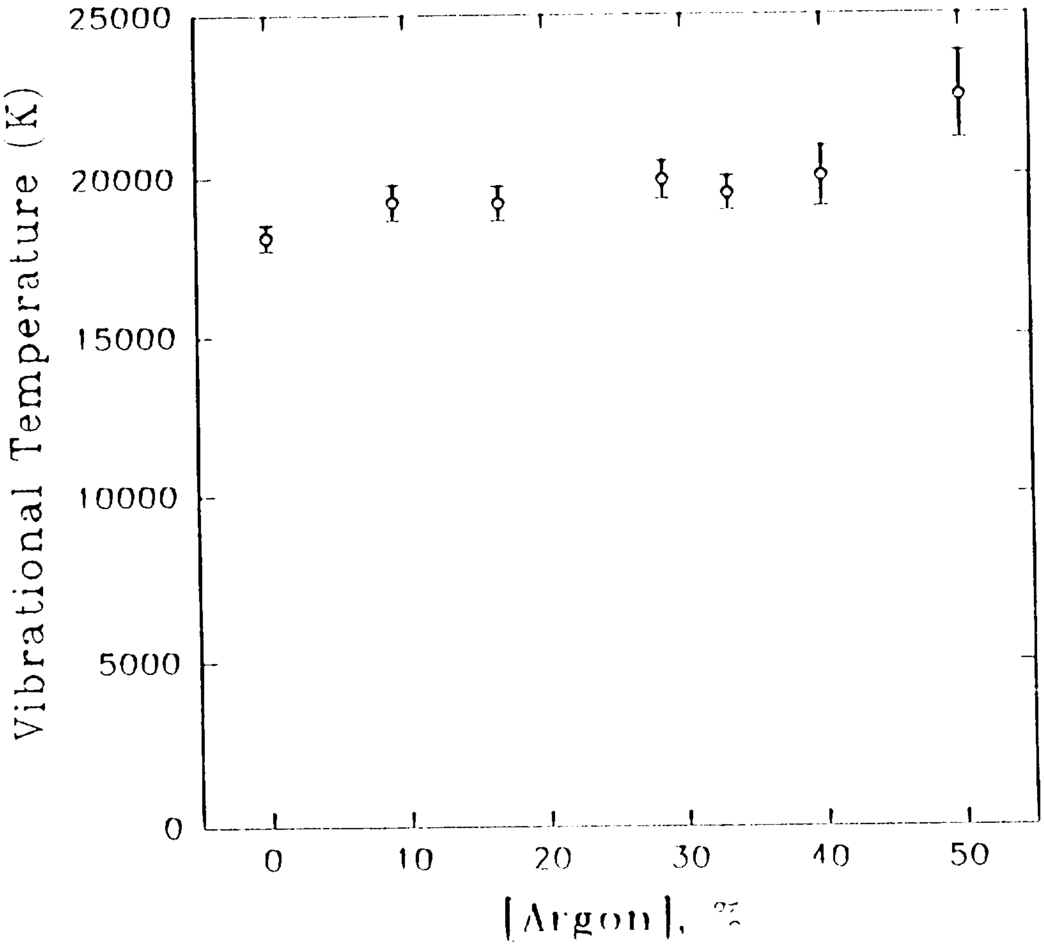

Figure 35. The vibrational temperature versus the content of argon.

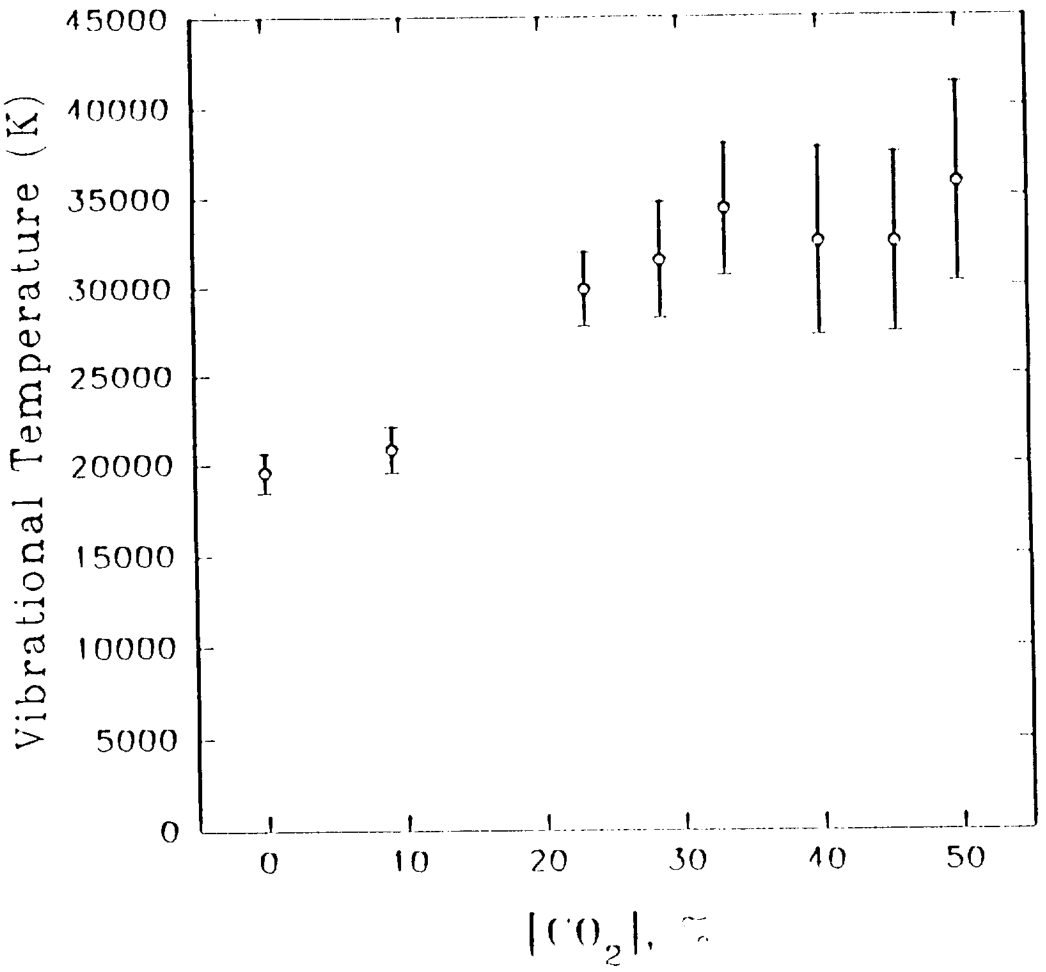

Figure 36. The vibrational temperature versus the content of CO$_2$.

5. SUMMARY AND CONCLUSION.

The study was aimed to measure N_2^+ emission spectra produced by the helium Penning ionization and to determine the vibrational and rotational temperatures. Also possible argon and CO_2 effects on N_2^+ emission was evaluated. The $B^2\Sigma_u^+$ state of molecular nitrogen ions was generated in a hollow-cathode discharge chamber by the collision of helium at the metastable state with nitrogen molecule. When the $B^2\Sigma_u^+$ state of N_2^+ decays to the $X^2\Sigma_g^+$ state, a line emission at 391.44 nm is produced. The metastable state of helium (He^*) was monitored by probing the emission spectrum at 388.91 nm which is emitted from the transition 3^3P to 2^3S. Under the conditions of 1.0 torr of helium pressure, 30 SCCM of nitrogen flowrate, 500 V of discharge voltage, and 3.75 mA of discharge current, sufficiently high intensity of N_2^+, B-X (0,0) and (1,0) lines were emitted with small fluctuation enabling a high resolution spectroscopy.

The spectrometer/OMA system was calibrated with EG & G GS 900 standard light source for the absolute intensity measurement. The measured irradiance showed a trend of increase as the input current, helium pressure, and nitrogen flowrate were increased. Most of the collisions of nitrogen molecules by the He^* were occurred at the ±2 mm region from the nitrogen injector. With the 50% argon or CO_2 mixture, the irradiance was reduced by 34% and 78%, respectively. These results lead to a conclusion that there are no significant effects on N_2^+ emission of argon and CO_2 at the upper atmosphere flight region for their small (< 1%) concentrations.

The rotational temperature was determined from the Boltzmann plot by the resolved rotational lines of N_2^+, B-X (0,0) bandhead. For the possible errors embedded into the measured data, the error sources, such as, the intensity fluctuation, overlap of R-branch with P-branch, and the line-of-sight averaging, were recognized and considered in the data reduction. The overall experimental error was less than ±9.5%. The rotational temperatures were in the range of 300 to 370 K, and did not show any appreciable change against the substantial changes in helium pressure, current, nitrogen flowrate, detection position, and the content of argon and CO_2.

The vibrational temperature was determined by the relation of the absolute intensities of N_2^+, B-X (0,0) and (1,0) lines. The range of the estimated vibrational temperature was 18,000 to 36,000 K with argon or CO_2 mixture. With the 50% argon or CO_2 mixture, the vibrational temperature was increased by 24.1% and 82.9%, respectively. The results of vibrational temperature estimation again indicate that a small amount of argon and CO_2

have insignificant effects on the vibrational temperature at the upper atmosphere flight region. However use of a large concentration of these gases in the ground test facilities requires an account of their effects on N_2^+ kinetics. The results of the vibrational and rotational temperatures from this experiment are in contrast to the model by the CFD codes used for simulating hypersonic shock layer which results rotational temperature higher than vibrational one. Such nonequilibrium was also found with the argon or CO_2 mixture for which the vibrational temperature was increased while the rotational temperature remained constant.

In conclusion, we found that the excited N_2^+ generated by the helium Penning ionization was thermally nonequilibrium with significantly different rotational and vibrational temperatures. The nonequilibrium nature was also confirmed by the argon or CO_2 mixture verifying that heavy-particle inelastic collisions, such as Penning ionization used here and photoionization observed by others, transfer energy preferentially to the vibrational mode over the rotational mode.

REFERENCES

1. J. J. Jones, The rationale for an aeroassist flight experiment, AIAA Paper 87-1508 (1987)
2. P. A. Gnoffo, R. N. Gupta, J. Shinn, Conservation equations and physical models for hypersonic air flows in thermal and chemical nonequilibrium, NASA TP 2867, (1989)
3. L. C. Hartung, Development of a nonequlibrium radiative heating prediction methods for coupled flowfield solutions, J. of Thermophysics and Heat Transfer, **6**, 618 (1992)
4. L. C. Hartung et al., Stagnation point nonequilibrium radiative heating and the influence of energy exchange models, J. of Thermophysics and Heat Transfer, **6**, 412 (1992)
5. C. Laux, S. Moreau, and C. Kruger, Experimental study and improved modeling of high-temperature air radiation, AIAA Paper 92-2969 (1992)
6. F. M. Penning, Naturwise, **15**, 818 (1927)
7. Z. Herman and V. Cermak, Coll. Czech. Chem. Commun., **31**, 649 (1966)
8. H. Hotop and A. Niehaus, J. Mass Spectrum and Ion Physics, **5**, 415 (1970)

9. W. C. Richardson and D. W. Setser, Penning ionization opticalspectroscopy, J. Chemical Physics, **58**, 1809 (1973)
10. M. Cher and C. S. Hollingsworth, Chemiluminescent reaction of He(2^3S) with Nitrogen, Oxygen, Carbon Monoxide, and Carbon Dioxide, J. Chem. Phys., **50**, 4942 (1968)
11. F. Howorka, J. Chem. Phys., **68**, 804 (1978)
12. N. G. Adams, A. G. Dean, and D. Smith, Int. J. Mass Spectrum. Ion Phys., **10**, 63 (1972)
13. D. Hyatt and P. F. Knewstubb, J. Chem. Soc. Faraday Trans., **68**, 202 (1972)
14. W. Lindinger, F. Howorka, P. Lukac, H. Villinger, E. Alge, and H. Ramler, Phys. Rev., **23**, 2319 (1981)
15. R. C. Boldon, R. S. Hemsworth, M. J. Shaw and N. D. Twiddy, The measurement of Penning ionization cross sections for helium 2^3S metastables using a steady-state flowing afterglow method, J. Physics, **3**, 61(1970)
16. K. L. Bell, A. Dalgarno, A. E. Kingston, Penning ionization by metastable helium atoms, J. Phys. B, **1**, 18 (1968)
17. G. Herzberg, Molecular spectrum and molecular structure; I. Spectra of diatomic molecules, National Research Council of Canada, 468 (1950)
18. H. E. Blackwell, E. Yuen, S. Arepalli, C. D. Scott, Nonequilibrium shock layer temperature profiles from arc jet radiation measurements, AIAA Paper, 89-1670, (1989)
19. H. E. Blackwell and C. D. Scott, Measured rotational and vibrational temperature differences in arc jet shock layer, AIAA Paper 92-3030 (1992)
20. S. P. Sharma and W. Gillespie, Nonequilibrium and equilibrium shock front radiation, AIAA Paper, 90-0139 (1990)
21. C. R. Brundle, A. D. Baker, Electron spectroscopy : Theory, Techniques and Applications, Academic Press INC., London, 199 (1984)
22. J. D. Cobine, Gaseous Conductors, McGraw-Hill, New York, 214 - 218 (1941)
23. G. Herzberg, Atomic spectra and atomic structure, Dover Publications, New York (1944)
24. N. G. Adams and D. Smith, Product-ion distribution for some ion-molecule reaction, J. Phys. B, **9**, 1439 (1976)
25. G. Herzberg, Molecular spectrum and molecular structure; I. Spectra of diatomic molecules, National Research Council of Canada, 124 - 127 (1950)
26. J. Richter, Plasma diagnostics, W. Lochte-Holtgreven Pub. Comp., 15 (1968)
27. R. A. Sanders, A. N. Schweid, M. Weiss and E. E. Muschlitz, Jr., Velocity dependence of sensitized fluorescence in collisions of metastable argon and helium atoms with nitrogen, J. Chem. Phys., **65**, 2700 (1976)
28. C. Mark and C. S. Hollingworth, Chemiluminescent reaction of He with nitrogen, oxygen, carbon monoxide, and cabon dioxide, J. Chem. Phys., **50**,

4942 (1969)
29. J. Glosik, A. B. Rakshit, N. D. Twiddy, N. G. Adams, and D. Smith,Measurement of the rates of reaction of the ground and metastable excitestates of O_2^+, NO^+, and O^+ with atmospheric gases at thermal energy, J. Phys., 11, 3365 (1978)
30. J. M. Seitzmann, Quantitave applications of fluorescence imaging in combustion, Ph. D. Thesis, Department of Mechanical Engineering, Stanford University (1990)31. L. M. Cohen, Emission and laser-induced fluorescence diagnostics of a supersonic jet of plasma-heated nitrogen, Ph. D. Thesis, Department of Mechanical Engineering, Stanford University (1991)
32. J. L. Palmer, Method of characteristics for two-dimensional, steady supersonic flow of a thermally perfect gas applied to flow in supersonic nozzles and underexpanded free jets, High Temperature Gasdynamics Laboratory, Stanford University.
33. A. T. Schonemann, N. K. Auweter, H. A. Habiger, P. C. Sleziona, T. Stockle, Experimental and numerical investigation of the influence of argon used as protection gas in a reentry simulation device, Draft AIAA Paper (1993)
34. M. R. Torr, D. G. Torr, P. G. Richards, The N_2^+ first negative system in the dayglow from Specelab 1, J. Geophys. Res., 97, 17075 (1992)
35. J. L. Cambier, S. Moreau, Simulations of a molecular plasma in collisional-radiative nonequilibrium, AIAA Paper 93-3196 (1993)